DivIVA controls the dynamics of septum splitting and cell elongation in *Streptococcus pneumoniae*

Jennyfer Trouve[1], André Zapun[1], Laure Bellard[1], Dimitri Juillot[2], Anais Pelletier[3], Celine Freton[3], Morgane Baudoin[4], Rut Carballido-Lopez[2], Nathalie Campo[5,6], Yung-Sing Wong[4], Christophe Grangeasse[3] and Cecile Morlot[1,*]

[1] Univ. Grenoble Alpes, CNRS, CEA, IBS, 38000 Grenoble, France.
[2] Université Paris-Saclay, INRAE, AgroParisTech, Micalis Institute, 78350, Jouy-en-Josas, France.
[3] Molecular Microbiology and Structural Biochemistry (MMSB), CNRS, Univ. Lyon 1, UMR 5086, Lyon 69007, France.
[4] Univ. Grenoble Alpes, CNRS, DPM, 38000 Grenoble, France.
[5] Laboratoire de Microbiologie et Génétique Moléculaires, UMR5100, Centre de Biologie Intégrative, Centre Nationale de la Recherche Scientifique, 31062 Toulouse, France.
[6] Université Paul Sabatier (Toulouse III), 31062 Toulouse, France.

* Correspondence: cecile.morlot@ibs.fr

Running title: role of DivIVA in ovococci morphogenesis

ABSTRACT

Bacterial shape and division rely on the dynamics of cell wall assembly, which involves regulated synthesis and cleavage of the peptidoglycan. In ovococci, these processes are coordinated in an annular mid-cell region with nanometric dimensions. More precisely, the cross-wall that is synthesized by the divisome is split to generate lateral wall, whose expansion is insured by insertion of so-called peripheral peptidoglycan by the elongasome. Septum cleavage and peripheral peptidoglycan synthesis are thus crucial remodeling events for ovococcal cell division and elongation. The structural DivIVA protein has long been known as a major regulator of these processes but its mode of action remains unknown. Here, we integrate click chemistry-based peptidoglycan labeling, direct stochastic optical reconstruction microscopy and in silico modeling, as well as epifluorescence and stimulated emission depletion microscopy to investigate the role of DivIVA in *Streptococcus pneumoniae* cell morphogenesis. Our work reveals two distinct phases of peptidoglycan remodeling along the cell cycle, that are differentially controlled by DivIVA. In particular, we show that DivIVA ensures homogeneous septum cleavage and peripheral peptidoglycan synthesis around the division site, and their maintenance throughout the cell cycle. Our data additionally suggest that DivIVA impacts the contribution of the elongasome and class A PBPs to cell elongation. We also report the position of DivIVA on either side of the septum, consistent with its known affinity for negatively curved membranes. Finally, we take the opportunity provided by these new observations to propose hypotheses for the mechanism of action of this key morphogenetic protein.

IMPORTANCE

This study sheds light on fundamental processes governing bacterial cell growth and division, using integrated click chemistry, advanced microscopy and computational modeling approaches. More precisely, it addresses mechanisms involved in the regulation of cell wall synthesis and remodeling in *Streptococcus pneumoniae*. This bacterium belongs to the morphological group of ovococci, which includes many human pathogens, such as streptococci and enterococci. In this study, we have dissected the function of DivIVA, which is a structural protein involved in cell division, cell morphogenesis and chromosome partitioning in Gram-positive bacteria. This work unveils the role of DivIVA in the orchestration of cell division and elongation along the pneumococcal cell cycle. It not only helps understanding how ovoid bacteria proliferate, but also offers an opportunity to consider how DivIVA

might serve as a scaffold and sensor for particular membrane regions, and thus be involved in various processes associated with the cell cycle.

KEYWORDS

Cell morphogenesis, cell division, cell elongation, peptidoglycan, cell wall, DivIVA, *Streptococcus pneumoniae*, ovococci, click chemistry, super-resolution microscopy, dSTORM, stimulated-emission-depletion microscopy.

INTRODUCTION

Peptidoglycan (PG) is a three-dimensional network made of repeated *N*-acetylglucosamine-*N*-acetylmuramic acid disaccharide units cross-linked by short peptides (Vollmer et al., 2008a). PG confers resistance to turgor pressure and a specific cellular shape adapted to the environment of the bacterium. This shape is tuned by the dynamics of PG synthesis and remodeling (Pinho et al., 2013; Trouve et al., 2021b), whose enzymatic actors are well known but whose organizational and regulatory factors remain poorly understood.

Assembly of the PG at the cell surface is performed by transglycosylase activities, which polymerize the PG precursor unit lipid II (a membrane-anchored disaccharide pentapeptide) into glycan chains, and by transpeptidase activities, which crosslink the peptide chains. PG synthases include SEDS proteins (Shape, Elongation, Division and Sporulation), which carry transglycosylase activities, and Penicillin-Binding Proteins (PBPs) (Meeske et al., 2016; Sauvage et al., 2008). Class A PBPs (called aPBPs henceforth) are bifunctional enzymes carrying both transglycosylase and transpeptidase domains, while class B PBPs (bPBPs) are monofunctional transpeptidases (Meeske et al., 2016; Sauvage et al., 2008). bPBPs work in tandem with a cognate SEDS protein and participate to the cell division or cell elongation complexes called the divisome or the elongasome, respectively (Käshammer et al., 2023; Reichmann et al., 2019; Sjodt et al., 2020; Taguchi et al., 2019; Zapun et al., 2012). aPBPs work independently from these two machineries, presumably filling in gaps and/or densifying the PG mesh (Cho et al., 2016; Straume et al., 2021; Vigouroux et al., 2020). PG remodeling on the other hand involves hydrolytic activities that cleave specific bonds within the nascent PG, allowing for example daughter cell separation or insertion of new material into the PG network (Vollmer et al., 2008b).

89 In this work, we investigated PG synthesis and remodeling in the opportunistic human
90 pathogen *Streptococcus pneumonia*e. This bacterium belongs to the morphological group of ovococci
91 (*e. g*. streptococci and enterococci), whose shape results from septal and peripheral PG syntheses,
92 which respectively allow cell division and cell elongation (Briggs et al., 2021; Zapun et al., 2008). In *S.*
93 *pneumoniae*, the divisome and elongasome contain the bPBP2x/FtsW and bPBP2b/RodA pairs,
94 respectively (Briggs et al., 2021; Perez et al., 2019; Philippe et al., 2014; Straume et al., 2017; Zapun
95 et al., 2012). None of the three pneumococcal aPBPs (aPBP1a, aPBP2a and aPBP1b) is essential but
96 inactivation of both aPBP1a a and aPBP2a is lethal (Paik et al., 1999). Furthermore, aPBP1a
97 modifies septal PG synthesized by the PBP2x/FtsW divisome pair (Straume et al., 2020). PG
98 hydrolases related to cell division include the amidase/endopeptidase PcsB, the glucosaminidase
99 LytB, and the muramidase Pmp23/MpgB (Bai et al., 2014; Barendt et al., 2009; Bartual et al., 2014;
100 De Las Rivas et al., 2002; Jacq et al., 2018; Taguchi et al., 2021). On the other hand, the muramidase
101 MltG/MpgA works in conjunction with the elongasome (Tsui et al., 2016).
102 Because PG synthetic and hydrolytic activities happen in regions with nanometer-scale
103 dimensions, investigating their dynamics requires super-resolution microscopy methods that break
104 the light diffraction barrier (Schermelleh et al., 2019). Recently, the combination of click-chemistry
105 bio-orthogonal labeling with dSTORM (direct Stochastic Optical Reconstruction Microscopy) and *in*
106 *silico* modeling improved our understanding of cell morphogenesis in the ovoid-shaped bacterium *S.*
107 *pneumoniae* (Trouve et al., 2021b, 2021a). Proteins in charge of septal and peripheral PG synthesis
108 are recruited to mid-cell by the cytoskeletal protein FtsZ at the beginning of the cell cycle, and their
109 activities are first confounded within an annular region whose nanometric dimensions approximate
110 that of the ring formed by FtsZ (Jacq et al., 2015; Trouve et al., 2021b). Later on, two synthesis
111 regions progressively separate, the inner one corresponding to septal PG synthesis and the outer
112 one to peripheral PG (Fig. S1A) (Perez et al., 2021; Trouve et al., 2021b). Importantly for this work,
113 the study of PG dynamics by dSTORM brought support to a mechanism in which PG synthesis by the
114 divisome at the membrane invagination front forms a septal matrix that is split at its periphery by
115 hydrolases to form the new cell hemispheres. Peripheral PG is inserted by the elongasome at the
116 periphery of the septum, into freshly cleaved septal material or concomitantly with the cleavage
117 (Fig. S1A) (Trouve et al., 2021b). In this model, septum remodeling through cleavage and
118 incorporation of peripheral PG would thus be a key event allowing both cell separation and cell
119 elongation. Because they modify septal PG, aPBPs probably also influence septum cleavage and/or
120 peripheral PG insertion (Straume et al., 2020).

121 With regards to the mechanisms of septum remodeling, the membrane-associated coiled-coil
122 protein DivIVA is thought to be a main player (Halbedel and Lewis, 2019; Hammond et al., 2019).
123 In *S. pneumoniae*, DivIVA is found at the division site and the cell poles, and it interacts with many
124 elongation and division proteins, including bPBP2x, bPBP2b and aPBP1a (Fadda et al., 2007; Fleurie
125 et al., 2014; Hammond et al., 2019; Straume et al., 2017). Deletion of the *divIVA* gene results in
126 chains of short pneumococcal cells, indicative of impaired cell separation and elongation (Fadda et
127 al., 2003; Fleurie et al., 2014; Straume et al., 2017). In *Streptococcus suis*, DivIVA interacts with
128 MltG/MpgA and its absence causes a cell elongation defect (Jiang et al., 2023). Altogether, these
129 observations point to a functional link between DivIVA and cell growth, but its exact function
130 remains unknown.

131 Here, we used state-of-the-art fluorescence microscopy methods to investigate the role of
132 DivIVA in *S. pneumoniae* cell morphogenesis. Using conventional fluorescence microscopy and
133 STED (stimulated-emission-depletion), we describe the localization of DivIVA on both sides of the
134 division site. Importantly, by combining bio-orthogonal PG labeling, dSTORM imaging and *in silico*
135 modeling to analyze PG synthesis in *divIVA* mutants, we reveal that the dynamics of septum
136 remodeling displays two phases along the pneumococcal cell cycle. During these two phases,
137 DivIVA promotes both splitting of the septum and peripheral PG synthesis, ensuring that these two
138 activities are synchronous around the septal periphery and maintained all along the division cycle.

139

140

141 # RESULTS

142 **DivIVA localizes as a double ring at constricting division sites**

143 Several studies have shown that DivIVA localizes at the division site in various bacterial species and
144 in some cases at the cell poles, including in *S. pneumoniae* (Cramer et al., 2024; Fadda et al., 2007;
145 Fleurie et al., 2014; Sutton et al., 2023). To further document the localization and dynamics of the
146 pneumococcal DivIVA, we constructed a functional DivIVA-HT fusion at the endogenous *divIVA*
147 locus (Fig. S2). Observation of DivIVA-HT using conventional fluorescence microscopy confirmed
148 its septal and polar localization (Fig. 1A). Interestingly, it also showed an enrichment of the protein
149 at mid- and late-division sites (constricting sites) compared with early-division sites (non-
150 constricted sites) and cell poles (Fig. 1B). The localization of DivIVA at mid-cell is thus correlated
151 with division stages during which the septum is being remodeled (Trouve et al., 2021b).

152 STED microscopy further revealed the localization of DivIVA as a double band at mid-cell (Fig. 1C-
153 D). These double bands, which correspond to the 2D projection of rings, are separated by a median
154 distance of 93 ± 13 nm (n = 14).
155
156 **DivIVA affects the dynamics of the pneumococcal cell cycle**
157 In the absence of DivIVA, *S. pneumoniae* cells are still able to form complete septa but they do not
158 cleave them efficiently, forming chains of more than 70 µm (Fig. 2A) (Fadda et al., 2007; Fleurie et
159 al., 2014; Straume et al., 2017). To further characterize these defects, we analyzed the Δ*divIVA*
160 strain by dSTORM following a short labeling pulse with the azido-D-Ala-D-Ala (aDA-DA) probe,
161 which is incorporated into the growing PG (Trouve et al., 2021b, 2021a). The labeled cell chains
162 display band-like patterns that result from the 2D projection of annular PG synthesis regions. The
163 length of the labeled bands therefore measures the outer diameter of the pulse-labeled synthesis
164 rings. Since they do not separate, the cells of the Δ*divIVA* strain could not be classified along the cell
165 cycle as routinely performed with the wild-type (WT) strain (Fig. S1B) (Trouve et al., 2021b).
166 Instead, we sought to classify the labeled PG synthesis sites. We observed an alternation of
167 constricted and non-constricted labeling bands of various intensities (Fig. 2A). Interpreting the
168 parental relationships between bands was complicated by the fact that a given site is not
169 necessarily surrounded by sites of a single generation, but can also be bracketed by sites of
170 different generations (Fig. 2B). We therefore based our classification on the diameter of the site
171 considered with respect to that of its neighbors (Fig. 2C). We identified three classes of PG
172 synthesis sites: the early-division class (E) harbors large diameters (> 800 nm) and no visible
173 constriction, the mid-division group (M) exhibits visible constriction (d_M) and neighboring sites that
174 are even more constricted ($d < d_M$), and the late-division group (L) includes constricted sites (d_L)
175 flanked by sites that are less constricted ($d > d_L$). Our analysis revealed that most of the PG
176 synthesis sites fall into the late-division group in the Δ*divIVA* strain, with 30%, 17% and 53% (n =
177 200) of the sites assigned to the early-, mid- and late-division classes, respectively (Fig. 2D). To
178 compare these proportions with that of the WT strain, the cell categories reported previously were
179 converted into categories of labeled bands by adding two early-division sites for each late division
180 cell (Fig. S1B), since these were defined as displaying a constricted site surrounded by two new
181 daughter sites (Trouve et al., 2021b). The division sites of the WT strain are thus distributed with
182 proportions of early-, mid- and late-division of 68, 18 and 14%, respectively. Since cells were
183 labeled during steady-state growth, the proportion of each labeled sites reflects the relative
184 duration of the corresponding stage of the cell cycle. In the absence of DivIVA, the late-division

185 stage is therefore longer than the earlier stages. Consistent with this observation and with a defect
186 in septum splitting, the median diameters of the labeling sites in the Δ*divIVA* strain are higher than
187 in the WT strain (Fig. 2E).
188 Quantification of the number of localizations further shows that compared to the WT strain,
189 less PG is synthesized in the absence of DivIVA (Fig. 2F). Whereas PG insertion remains robust
190 along the whole cell cycle of WT cells, it dwindles to 27% of its maximum during late-division
191 stages when *divIVA* is deleted. Also of note, the shortest labeled diameters measured in WT cells
192 are at 150 nm, whereas the smallest diameter in the absence of DivIVA is about 280 nm (Fig. 2E). It
193 is unclear whether cells fail to complete their cell division or if it continues at an extremely slow
194 rate at which labeling is not detected.
195
196 **The pneumococcal cell cycle consists of two elongation phases**
197 When scanning Δ*divIVA* cell chains, symmetrical patterns, sometimes of up to seven bands, can be
198 found (Fig. 3). This number indicates that following a round of division, the cell cycles of the
199 descendants can remain synchronized for two more rounds of division (see Fig. 2B). Labeling
200 bands arising from a fourth generation are much less frequent, implying that the rate of cell cycle
201 progression between cells vary sufficiently to nullify synchronization beyond three or four
202 generations. We distinguished four typical symmetrical patterns. In one pattern (Fig. 3A), four long
203 weakly-labeled bands (grey arrowheads, early stages) surround a short middle weakly-labeled
204 band (central orange arrowhead, late stage) and two strongly-labeled bands of intermediate length
205 (lateral orange arrowheads, late stage). In the second pattern (Fig. 3B), the central weakly-labeled
206 band (central orange arrowhead, late stage) is flanked by four strongly-labeled bands (grey
207 arrowheads, early stages), which sandwich two bands of smaller diameter (lateral orange
208 arrowheads, late stages). The third pattern (Fig. 3C) is similar to the previous one, but the two
209 small diameter bands show a weak labeling. A fourth pattern shows a series of weakly labeled
210 bands (Fig. 3D).
211 To understand the dynamics of PG synthesis underlying the observed dSTORM patterns, we
212 previously developed a dynamic geometrical model of cell wall expansion. This model was
213 parametrized using measurements taken on experimental data and could successfully recapitulate
214 the labeling patterns of the WT strain (Fig. S1B) (Trouve et al., 2021b). Interestingly, to reproduce
215 the patterns obtained with the Δ*divIVA* strain, this model had to be refined. Whereas modeling data
216 from WT strains required an acceleration of the elongation rate to account for the thickening of the
217 labeling bands along the cell cycle (Trouve et al., 2021b), the statistics of the band diameters and

218 number of localizations measured for the Δ*divIVA* mutant (Fig. 2E-F) suggested a deceleration of
219 the cell elongation. Different functions were trialed to model a deceleration of the elongation rate,
220 but the morphology of the Δ*divIVA* strain and the labeling patterns could best and most simply be
221 mimicked with two successive phases of constant elongation rates. Two additional parameters
222 were thus added to the model to define when the second phase starts, and how reduced is its rate
223 compared to the first phase. The absence of small labeled rings was modeled by a complete stop of
224 the cell cycle at a fraction of the full cell length. The other parameters of the model remain.
225 Regarding the cells, they are the length/diameter ratio, the time of completion of the septum
226 closure and the time of the start of the next generation. Regarding the labeling patterns, the
227 parameters are the start and the length of the pulse. In contrast to the WT strain for which the
228 values of the parameters were obtained by fitting of the model functions to experimental
229 measurements (Trouve et al., 2021b), the number of measurable, well-defined symmetrical
230 patterns of the different types was not sufficient to perform meaningful fitting. Instead, the values
231 of the parameters were manually adjusted to best represent the Δ*divIVA* observations. The
232 modeled labeling patterns and cell wall representations are shown alongside dSTORM images in
233 Fig. 3. The chosen values are given in Table 1. Graphs of the modeled evolution of the cell length,
234 outer and inner diameter of the septum with the chosen parameters are given in supplementary
235 Fig. S3. The first pattern (Fig. 3A) is produced when the labeling takes place when the second
236 generation (yellow arrowheads) is producing most of its septum whereas the septum of the first
237 generation (teal arrowhead) has already closed and the third-generation division has just started
238 (pink arrowheads) (see Fig. S3 for the position of the green labeling pulse). In the second pattern
239 (Fig. 3B), the pulse starts slightly later, while septum synthesis of the second generation is already
240 well advanced (Fig. S3, orange labeling pulse). To generate the third pattern (Fig. 3C), a short pulse
241 occurs as the third division cycle is in the first (fast) phase, whereas the second- and first-
242 generation cycles are in the second slower phase and after septal closure (Fig. S3, cyan labeling
243 pulse). The weak labeling is the result of slow peripheral PG insertion. The fourth pattern (Fig. 3D)
244 appears when the labeling pulse occurs while three successive divisions have closed their septum
245 and ceased to incorporate PG material but a fourth division (blue arrowheads) has just started (Fig.
246 S3, yellow labeling pulse). The experimental data acquired on the Δ*divIVA* strain are thus
247 consistent with a biphasic model of the pneumococcal cell cycle in which the elongation rate is
248 reduced during the second phase.
249

250 **Septal synthesis is maintained but septum splitting and peripheral synthesis are impaired in**
251 **the absence of DivIVA**

252 To further analyze the dynamics of PG synthesis in the Δ*divIVA* strain, we analyzed tilted cells
253 in which the radial architecture of the labeled regions can be observed (Fig. 4A). To account for the
254 difference in cell diameter between the WT and Δ*divIVA* strains, we normalized the width of the
255 septal plate (measured as the distance *r*, Fig. 4B) to the mean value of early-stage labeling
256 diameters ($d(E)_{WT}$ = 850 nm; $d(E)_{\Delta divIVA}$ = 980 nm), as those have not yet initiated constriction. At
257 mid- and late-division stages, the *r/d(E)* ratio is greater than in the WT strain (Fig. 4C), consistent
258 with active septal PG synthesis and defective septum splitting in Δ*divIVA* cells. In this orientation,
259 WT cells at mid- and late-division stages show inner and outer labeling rings, respectively
260 corresponding to septal and peripheral PG synthesis (Fig. 4A, patterns *d* to *f*) (Trouve et al., 2021b).
261 Cells harboring these concentric patterns represent 4% (n = 148) of the whole WT cell population.
262 In Δ*divIVA* cells, similar concentric patterns are observed in a larger proportion of the cell
263 population (15%, n = 148) (Fig. 4A, patterns *c* to *f*), which is consistent with impaired septum
264 splitting. Indeed, since septal PG is synthesized at the leading edge of the growing septum and
265 peripheral PG is synthesized at its periphery, deficient cleavage of the septum favors the separation
266 of the two sites of synthesis. The experimental labeling patterns were correctly reproduced when
267 septal synthesis was maintained until septum closure, and the rate of septum splitting and
268 concomitant peripheral PG insertion was severely reduced in a second phase of the cell cycle (Fig.
269 4A).

270 The dynamics of septum splitting and peripheral synthesis, or in other words cell elongation,
271 were previously documented for WT strains using pulse-chase labeling experiments (Trouve et al.,
272 2021b). Pulse-labeled PG is remodeled during the chase period, resulting in pulse-chase
273 localization patterns that are wider than pulse patterns. In our model of pneumococcal PG
274 synthesis, the septal PG is rapidly cleaved during early division, so that it is repositioned as
275 hemispheric wall almost immediately after synthesis (Fig. S1A) (Trouve et al., 2021b). In a WT
276 strain, when this stage (E) is observed in a pulse-chase experiment, the pulse-labeled PG splits into
277 two bands during the chase, due to synthesis of unlabeled PG at mid-cell (Fig. 5A, grey arrowhead).
278 At mid- (M) and late (L) division stages, septum cleavage lags behind septal PG synthesis, resulting
279 in septum formation. In a pulse-chase experiment, a labeled septum is formed during the pulse and
280 is cleaved during the chase. The cell wall that is repositioned laterally during the chase thus
281 contains a mixture of labeled septally-synthesized PG and unlabeled peripheral PG (Trouve et al.,
282 2021b). Such remodeling appears as "butterfly-like" patterns (Fig. 5A, pink and orange

283 arrowheads). Throughout the cell cycle, the rate of septal cleavage and peripheral PG insertion can
284 be assessed by measuring the "width of the chase" (W_{CHASE}), which is the distance separating the
285 external borders of the labeled patterns in pulse-chased cells (Fig. 5B).

286 During early division, the median width of the chased region in Δ*divIVA* cells ($W_{CHASE}(E)$ = 270
287 nm, n = 119) is rather similar to that of the WT strain ($W_{CHASE}(E)$ = 260 nm, n = 123) (Fig. 5C). By
288 contrast, W_{CHASE} is reduced in the absence of DivIVA at mid- ($W_{CHASE}(M)$ = 280 nm, n = 57) and in
289 particular at late-division ($W_{CHASE}(L)$= 80 nm, n = 162) when compared to the WT strain ($W_{CHASE}(M)$
290 = 415 nm, n = 122; $W_{CHASE}(L)$= 430 nm, n = 119). These measurements confirm that elongation
291 slows down dramatically during the cell cycle in the absence of DivIVA, whereas it accelerates in the
292 WT strain. The geometrical model correctly reproduces the observed chased patterns (Fig. 5D).
293 Only sites that were labeled early during the first phase of rapid PG synthesis show significant
294 parting of split labeled bands. Sites that were labeled late during the first (rapid) phase or during
295 the second (slow) phase show little splitting of the bands.

296 In addition to the double-band patterns described above, 10% of the Δ*divIVA* early-division
297 sites (n = 301) showed asymmetric separation of the labeled region, resulting in "Y-like"
298 localization patterns (Fig. 5E). This proportion is probably underestimated since it only includes
299 "Y-like" patterns correctly oriented in the XY plane and does not consider similar patterns oriented
300 in the Z axis. Asymmetric pulse-chase labeling patterns are never observed in early-division WT
301 cells, in which pulse-labeled regions are always chased as parallel bands (Fig. 5A). In the absence of
302 DivIVA, the presence of Y-like labelings indicate that septal splitting and associated peripheral PG
303 synthesis are non-uniformly distributed around the division site.

304

305 **The contribution of the elongasome and aPBPs to cell elongation is modified in the absence**
306 **of DivIVA**

307 *S. pneumoniae* cell elongation is known to rely on peripheral PG synthesis by the elongasome,
308 which is formed by the RodA/bPBP2b pair (Perez et al., 2021; Straume et al., 2017; Vollmer et al.,
309 2019). On the other hand, given that peripheral PG is inserted into cleaved septal regions and that
310 septal PG is modified by aPBPs (Straume et al., 2020; Trouve et al., 2021b), it is possible that aPBPs
311 influence peripheral PG insertion and thus cell elongation. Since the later process is impaired in
312 Δ*divIVA* cells, we sought to investigate the interplay between DivIVA and the elongasome or aPBPs
313 using pulse-chase experiments (Fig. 6A and 6C). Consistent with a previous study by Tsui et al,
314 deletion of *pbp2b* in a WT background required the combined inactivation of *mltG*, which was
315 obtained by mutating the catalytic tyrosine (Y488D mutation) (Tsui et al., 2016). Measurement of

316 W_{CHASE} was used to estimate the cell elongation. Compared to WT cells, W_{CHASE} is reduced by a factor
317 of 1.4, 1.5 and 1.6 at early-, mid- and late-division stages in Δ*pbp2b mltG*$_{Y488D}$ cells (Fig. 6B). In a WT
318 background, bPBP2b-based peripheral PG synthesis is therefore a major contributor to all
319 elongation phases. Interestingly, cell elongation is also diminished in mid- to late-division stages in
320 the absence of aPBP1a or aPBP2a.

321 As reported previously (Fleurie et al., 2014), we could not delete the *pbp2b* gene in the Δ*divIVA*
322 background, indicating that bPBP2b is still essential in the absence of DivIVA. As in a WT strain, we
323 had to inactivate MltG to suppress the requirement for bPBP2b. However, in the Δ*divIVA*
324 background, bPBP2b inactivation had a milder effect on cell elongation. Indeed, compared to
325 Δ*divIVA* cells, W_{CHASE} is either not reduced during early- and mid-division, or reduced by a factor of
326 1.2 at the late-division stage in Δ*divIVA* Δ*pbp2b mltG*$_{Y488D}$ cells (Fig. 6D). In the absence of DivIVA,
327 the elongasome contribution to the cell elongation is thus diminished all along the cell cycle.

328 The comparison of the width of the chase between Δ*divIVA* and Δ*divIVA* Δ*pbp1a* cells shows a
329 reduction in cell elongation at all stages of the cell cycle, especially in early- and late-division stages,
330 upon *pbp1a* deletion (Fig. 6D). This is slightly different from the WT strain, in which the absence of
331 aPBP1a has no effect on W_{CHASE} during early-division (Fig. 6B). In a WT genetic background, the
332 contribution of aPBP1a to early-elongation is probably masked by the strong contribution of the
333 elongasome. The contribution of aPBP1a to early-division is therefore revealed by the absence of
334 DivIVA, as the role of bPBP2b is minimal in this genetic background. In Δ*divIVA* cells, aPBP1a
335 appears important for cell elongation all along the cell cycle.

336 The situation is somewhat different for aPBP2a. In the presence of DivIVA, aPBP2a mainly
337 contributes to mid- and late-division stages (Fig. 6B). By contrast, in Δ*divIVA* Δ*pbp2a* cells, W_{CHASE}
338 does not decrease at these stages compared to Δ*divIVA* cells, indicating a decreased participation of
339 aPBP2a to cell elongation in the absence of DivIVA (Fig. 6D). On the other hand, when compared to
340 Δ*divIVA* cells, W_{CHASE} is reduced by a factor of 1.4 during early-division in Δ*divIVA* Δ*pbp2a* cells.
341 Here again, the role of aPBP2a during early cell elongation is therefore revealed in the absence of
342 DivIVA.

343 In conclusion, the absence of DivIVA affects not only peripheral PG synthesis by the
344 elongasome, but also the contribution of aPBP1a and aPBP2a to cell elongation.

345

346

347 **DISCUSSION**

348 DivIVA is anchored in the plasma membrane by an N-terminal motif composed of a hydrophobic
349 residue flanked by positively charged amino acids (Choukate and Chaudhuri, 2020; Oliva et al.,
350 2010). The central part of DivIVA forms coiled coils of varying length in different Gram-positive
351 species. It assembles as a tetramer formed by the antiparallel association of two parallel coiled-coil
352 dimers. Depending on the organism, there is an additional non-conserved C-terminal tail.
353 Tetramers of DivIVA from *Bacillus subtilis* were found to assemble *in vitro* into large lattice-like
354 structures (Oliva et al., 2010). Most importantly, DivIVA binds preferentially to negatively curved
355 membrane regions, which accounts for its concentration at the cell poles and as two rings bordering
356 the invaginating membrane, as previously reported for *B. subtilis* (Cramer et al., 2024), and
357 established in this work for *S. pneumoniae*.

358 As a scaffold protein with an affinity for negatively curved membranes, DivIVA may have been
359 used and reused by the mechanisms of evolution as a platform for processes that must occur at
360 such places in bacteria. For examples, DivIVA directs apical growth in corynebacteria and
361 mycobacteria (Kang et al., 2008; Letek et al., 2008), it participates indirectly to positioning of the
362 division site in *B. subtilis* by interacting with the Min system (Eswaramoorthy et al., 2011), and it is
363 involved in chromosome partitioning by positioning the ParB protein at poles (Giacomelli et al.,
364 2022). In ovococci such as *S. pneumoniae*, the absence of DivIVA causes major morphological
365 defects, as the Δ*divIVA* strain grows as chains of lentil-shaped cells, compressed in the direction of
366 the long axis (this work and (Fleurie et al., 2014; Straume et al., 2017)). DivIVA is thus required for
367 proper ovoid shape, but how does it fulfill its morphogenetic function?

368 Here, we have shown that in *S. pneumoniae*, DivIVA is more concentrated at the division site
369 than at the cell poles, suggesting that it plays a major function at the sites of active PG synthesis.
370 The current model proposes that the ovoid shape of *S. pneumoniae* results from a finely balanced
371 and interconnected synthesis of septal and peripheral PG, respectively required for cell division and
372 elongation. The latter is thought to result primarily from the action of the RodA/bPBP2b
373 glycosyltransferase/transpeptidase couple associated with the hydrolase MltG/MpgA. Indeed, the
374 absence of a functional elongasome (RodA/bPBP2b/MltG) engenders chains of shorter cells (this
375 work and (Berg et al., 2013; Straume et al., 2017)), and our dSTORM data show that elongation is
376 actually impaired at all stages of the cell cycle. Cells without DivIVA display a similar morphology,
377 but we show in this case that elongation is only impaired at mid and late stages of the cell cycle.
378 Surprisingly, in the same cells, the elongasome appears to be inactive in early and mid stages. Early
379 elongation in Δ*divIVA* cells must therefore rely on another machinery than that of the elongasome.
380 Observations made in aPBP mutants may shed some light on this. Indeed, in the absence of DivIVA,

381 our data reveal a contribution of aPBP1a and aPBP2a to early elongation that is not detected in an
382 otherwise WT background. Therefore, DivIVA seems to affect in some way the function of the
383 elongasome and aPBPs, whose contribution to cell elongation seems to compensate each other
384 during the early stage of the cell cycle.

385 Regardless of the enzymatic machineries involved, a major observation allowed by our
386 dSTORM data is the existence of two cell growth phases during the pneumococcal cell cycle, as the
387 absence of DivIVA does not affect early elongation (first phase) but dramatically impairs mid and
388 late growth stages (second phase). More precisely, septation proceeds normally during the second
389 phase but splitting of the septum and concomitant peripheral synthesis are drastically slowed
390 down, leading to chains of shorter cells. From different attempts at simulating the labeling patterns
391 with a geometrical model of the cell growth, it appears that the deceleration of septum splitting and
392 peripheral synthesis must be abrupt rather that gradual. Later, it is possible that the elongation
393 process ceases completely as no labeling of division sites of small diameter could be detected. Since
394 long Δ*divIVA* cell chains still have extremities, the division of some rare cells may proceed to
395 completion through septal splitting possibly decoupled from peripheral synthesis. Alternatively,
396 long chains may be broken by the occasional lysis of some cells.

397 Also very interestingly, the resolution attained by dSTORM in pulse-chase labeling experiments
398 has revealed Y-shaped labeling patterns in Δ*divIVA* cells, while pulse-labeled regions are always
399 chased as parallel labeling rings in WT cells. These observations suggest that during the chase time,
400 the elongation due to septal splitting and peripheral synthesis sometimes progresses at different
401 speeds along the perimeter of the septum in the Δ*divIVA* strain, whereas the rate of elongation is
402 identical around the septal circumference in WT cells.

403 Our detailed dSTORM localization of PG assembly in a *divIVA* deletion strain thus shows that
404 DivIVA is necessary i) to maintain elongation passed a threshold time point during the cell cycle,
405 and ii) to coordinate the related processes around the mid cell perimeter. How can DivIVA achieve
406 such temporal and spatial regulation? Interestingly, the bi-phasic elongation process evidenced in
407 this work is reminiscent of the bi-phasic dynamic behavior of DivIVA, which was shown to move in
408 a directed manner around early-division sites and more diffusively around mid- and late-division
409 sites (Perez et al., 2019). A hypothesis that would unify all the observations reported to date would
410 thus be to consider that DivIVA is a physical sensor of membrane curvature, which would guide its
411 localization in regions where septum splitting and peripheral synthesis need to be stimulated.

412 Let us first consider how should evolve the force that favors septum splitting (Fig. 7A). The
413 surface tension resulting from the turgor pressure ΔP is $\gamma = \Delta PR/4$ where R is the radius of

414 curvature. At the junction of the septal and peripheral surfaces, for every segment s of the
415 circumference of the septum, this surface tension generates a force, tangential to the peripheral
416 surface away from the septum with a value $|\vec{F}_s| = \gamma s$. This force can be decomposed in a component
417 parallel to the septal plane $|\vec{F}_{||}| = \cos\theta|\vec{F}_s|$, and a component perpendicular to the septal plane $|\vec{F}_{\perp}| =$
418 $\sin\theta|\vec{F}_s|$, where θ is the angle between the new peripheral wall and the septal wall. This angle is
419 π/2 at the start and increases towards π at the end of the division. Therefore, the component
420 perpendicular to the septal plane $\vec{F}_{\perp}$, which should help tearing apart the septum, progressively
421 vanishes as the division progresses. A good analogy of this phenomenon is the removal of an
422 adhesive tape from a surface: it is easier if you pull perpendicularly to the surface than if you pull at
423 a shallow angle. Thus, the turgor pressure and the cell geometry provide a force $\vec{F}_{\perp}$ that can help
424 septum splitting. The stretched septal PG at the periphery could be a better substrate for the
425 cleaving enzyme.

426 The fact that in the absence of DivIVA, septum splitting and associated peripheral PG synthesis
427 proceed normally during early division and then slows dramatically, suggests that a different or
428 autonomous driving force exists at the beginning but is not present at the end of the process. The
429 mechanical force $\vec{F}_{\perp}$ described above could fulfill this role since it diminishes necessarily during cell
430 separation (Fig 7A). This waning force could reach a threshold where it is not sufficient and DivIVA
431 would kick-in to stimulate further septum splitting. DivIVA, by virtue of its affinity for negatively
432 curved membranes would be pre-localized exactly where required. In this scheme, DivIVA may be
433 considered as an activator of septum splitting and the associated peripheral PG synthesis. How
434 DivIVA achieves such activation remains mysterious. One common hypothesis is to propose that
435 DivIVA acts as a platform protein that interacts directly or indirectly with proteins of the cell wall
436 metabolism to concentrate them and/or activate them at specific locations. Based on the defective
437 peripheral synthesis observed in Δ*divIVA* cells, elongasome proteins appear as putative partners of
438 DivIVA. In agreement with this idea, DivIVA was shown to localize (but not activate) MltG/MpgA
439 through a direct physical interaction in *Streptococcus suis* (Jiang et al., 2023). MltG/MpgA might
440 thus use DivIVA as a localization platform. This hypothesis seems less likely for bPBP2b as it
441 remains localized in the absence of DivIVA, but we cannot exclude that DivIVA induces local
442 variations in bPBP2b concentrations that were not detected in the study by Fleurie et al (Fleurie et
443 al., 2014). An alternative hypothesis would be that DivIVA might indirectly activate peripheral
444 synthesis, again through a physical mechanism based on its negative-curve-affinity (Fig 7B). Let us
445 assume two additional features for DivIVA: a resting conformational angle ϕ_{rest} in the longitudinal
446 plane comprised somewhere between π/2 and π, and anchoring points to the cell wall at both

447 extremities (through some relay proteins). At the beginning of the division, the DivIVA angle would
448 be greater than that of the membrane at the periphery of the septum ($\phi = \phi_{rest} > \theta$). Since θ
449 increases as the septum is cleaved, at some point the DivIVA resting angle becomes smaller than
450 that of the membrane ($\phi_{rest} < \theta$) and DivIVA would be stretched ($\phi = \theta$). In this new configuration,
451 DivIVA experiences a tension that may be translated into an activation signal to interacting PG
452 synthases/hydrolases, or it could transfer tension to the periphery of the septal PG itself, taking
453 over the function of the diminishing splitting force $\vec{F}_{\perp}$. Note that the two hypothetical modes of
454 action are not mutually exclusive.

455 If the affinity of DivIVA for the membrane increases with the curvature, and if septum splitting
456 and peripheral synthesis are positively regulated by the presence of DivIVA, these two conditions
457 would ensure an orderly symmetrical proceeding of the division around the cell circumference. If
458 division were to occur faster in one region of the circumference (Fig. 7C right), the peripheral
459 membrane curvature in that region would become smaller than in the rest of the cell
460 circumference; the concentration of DivIVA would then decrease in this region of faster division
461 and increase elsewhere, where it would stimulate the process. The sliding and modification of the
462 local concentration of DivIVA along the septal circumference according membrane curvature would
463 thus automatically adjust the amount of cell wall metabolism required to ensure the even
464 progression of the division. In Δ*divIVA* cells, heterogeneous septum splitting and/or peripheral
465 synthesis would not be corrected by DivIVA, resulting in circularly asymmetrical PG labeling
466 profiles, observed as Y-shaped labeling patterns in our dSTORM images.

467 The biphasic dynamic behavior of DivIVA evidenced by Perez et al. can also be explained by its
468 affinity for negatively curved membranes (Perez et al., 2019). When the septum is not yet formed, if
469 FtsZ drives membrane invagination at the division site, places of maximal negative membrane
470 curvature necessarily follow the localization of the Z-ring around the cell perimeter. The affinity of
471 DivIVA for negative membrane curvature would result in DivIVA moving directionally around the
472 mid-cell circumference, seemingly "following" FtsZ treadmilling during early division. Past the very
473 early stage, a maximal negative curvature is established at the periphery of the septal plate,
474 whereas FtsZ remains localized at the leading edge of the closing septum. Consequently,
475 positioning of DivIVA would not depend on FtsZ treadmilling after the initial moments of the cell
476 division process. At these later stages, the localization of DivIVA molecules around the septal
477 periphery would depend on modulation of the negative curvatures resulting from septum splitting,
478 as proposed above.

479 Although the mode of action of DivIVA remains to be elucidated, our work improves our
480 understanding of the cell cycle in *S. pneumoniae* and highlights a regulatory function for DivIVA. It
481 sets the ground for further investigation, which should include cellular studies of DivIVA dynamics,
482 biophysical studies of DivIVA interaction with the membrane, as well as high-resolution structural
483 studies in the cell, such as cryo-correlative light and electron microscopy (cryo-CLEM), to correlate
484 the localization of DivIVA with the architecture of cellular ultrastructures.
485
486

487 # MATERIALS AND METHODS

488 ## Bacterial strains and growth conditions

489 The pneumococcal strains used in this study are listed in Table S1 and the strain construction is
490 described in *Supplementary Methods*. For PG labeling, 50 µL of glycerol stocks, frozen at OD_{600nm} =
491 0.3, were used to inoculate 1 mL of BHI medium. Cultures were grown at 37°C in a static CO_2
492 incubator, diluted twice into 10 mL of pre-warmed BHI medium (1/10th volume) to reach steady-
493 state growth, and treated for PG labeling when OD_{600nm} reached 0.3.

494 To localize DivIVA, cultures were inoculated at OD_{600nm} = 0.006 in C+Y medium and grown at 37°C
495 to an OD_{600nm} of 0.3. These cultures were diluted into C+Y medium (1/50th volume) and incubated at
496 37°C to an OD_{600nm} of 0.1. The cells were then incubated 10 min at 37°C with 20 nM HT-JFX646
497 ligand. For STED Microscopy, to fix the cells, 300 µL of culture were mixed with 100 µL of fixation
498 solution (0.5 M KPO_4 pH 7, 8% paraformaldehyde, 0.08% glutaraldehyde) and incubated for 15 min
499 at room temperature followed by 15 min on ice. Cells were then washed twice with 300 µL of 0.1 M
500 KPO_4 and finally concentrated 3 times. 0.8 µL of the cell suspension was immobilized on a 1.2% C+Y
501 agarose-coated microscopy slide with a cover glass (# 1.5) for cell imaging.
502

503 ## Epifluorescence and STED microscopy

504 Epifluorescence snapshots were performed on a previously described setup, equipped with a 100 x
505 objective and with laser excitation at 561 nm set at 30% of the maximum excitation power with
506 exposure time of 500 ms (Billaudeau et al., 2017). Demographs showing the fluorescence intensity
507 of DivIVA in relation to cell length was generated using MicrobeJ (version 5.13n), with specific
508 parameters previously reported (Juillot et al., 2024) : area (0.6-20 µm^2), length (0.5-max µm), width
509 (0.5-2 µm), circularity (0-1), curvature (0-max), sinuosity (0-max), angularity (0-0.25 rad), solidity

510 (0-0.85 max), and intensity (0-max). Cells with regular morphology that were initially excluded
511 from the segmentation due to proximity to other cells were included manually in the analysis.
512 Adjacent ovoid cells were meticulously examined to ensure accurate classification as one late-
513 division cell or two separated daughter cells. The resulting data were normalized as per MicrobeJ's
514 guidelines.
515 Heatmaps illustrating the average intensity of DivIVA-HT within cells was produced with MicrobeJ,
516 using cell categorization parameters previously reported as follows (Juillot et al., 2024): from left
517 to right, [SHAPE.length/SHAPE.width] ≤ 1.7; [SHAPE.length/SHAPE.width] > 1.7 and
518 [SHAPE.length] ≤ 1.6; [SHAPE.length/SHAPE.width] > 1.7 and [SHAPE.length] > 1.6;
519 [SHAPE.length/SHAPE.width] > 2 and [SHAPE.circularity] < 0.8; [SHAPE.length/SHAPE.width] > 2
520 and [SHAPE.circularity] < 0.7.

521 STED microscopy images were acquired with a STEDYCON (Abberior Instruments GmbH). Pulsed
522 laser at 640 nm was used for fluorescence excitation. A pulsed 775 nm STED depletion laser was
523 additionally used. The 640 nm excitation laser and the 775 nm depletion laser were set at 10% of
524 their maximum power. The optical setup was connected to an AxioImager Z2 fluorescence
525 microscope (Zeiss) with a 100× oil immersion PlanApochromat objective lens (NA = 1.46).
526 Acquisition software was STEDYCON Smart control. Measurements were performed with a pixel
527 dwell time of 10 µs.
528

529 **Preparation of PG labeling reagents**

530 All starting materials were obtained from commercial sources and were used without further
531 purification. NMR spectra were acquired on a Bruker Advance 400 MHz for ^{1}H-NMR experiments
532 and 100 MHz for ^{13}C-NMR experiments. Chemical shifts are reported in ppm (δ) relative to the
533 solvents: ^{1}H $\delta(CD_3OD)$ = 3.3 ppm, ^{13}C $\delta(CD_3OD)$ = 49.15 ppm. Accurate mass spectra were recorded
534 on a time-of-flight (TOF) spectrometer (Waters, XEVO G2-S QTof) and on a LTQ Orbitrap XL
535 spectromer with ElectroSpay Ionization (ESI, Thermo Scientific).

536 The aDA-DA probe (((*R*)-2-amino-3-azidopropanoyl)-D-alanine) was synthesized as previously
537 described (Trouve et al., 2021b). Briefly, 2-(trimethylsilyl)ethyl (*tert*-butoxycarbonyl)-D-alaninate
538 was obtained according to the Van Nieuwenhze's process and the (*R*)-3-azido-2-((*tert*-
539 butoxycarbonyl)amino)propanoic acid was obtained according to the Webb's process (described
540 for the L enantiomer) (Liechti et al., 2014; McAllister et al., 2011).

541 The N-Boc deprotection of 2-(trimethylsilyl)ethyl (*tert*-butoxycarbonyl)-D-alaninate was
542 performed in a solution of 4 N HCl in dioxane for 3 h to give, after removal of solvent, trituration in
543 dried ether, and drying under high vacuum (4 h), the corresponding salt in quantitative yield. This
544 latter and the (*R*)-3-azido-2-((*tert*-butoxycarbonyl)amino)propanoic acid (1.4 equivalent) were
545 dissolved in dry CH_2Cl_2. HATU (1.1 equivalent), di-isopropyl ethyl amine (DIPEA, 2.3 equivalent)
546 was added and the mixture was stirred overnight. After removal of the solvent, ethyl acetate was
547 added and the solution was washed with an aqueous solution of 10% citric acid followed by 5%
548 $NaHCO_3$. The combined organic layers were dried ($MgSO_4$) and evaporated. After purification flash
549 chromatography, the resulting 2-(trimethylsilyl)ethyl ((*R*)-3-azido-2-((*ter*-
550 butoxycarbonyl)amino)propanoyl)-D-alaninate was obtained in 63% yield. The final deprotections
551 were performed by addition of trifluoroacetic acid (TFA) at 0°C followed by stirring for 4 h at room
552 temperature. The solvent was evaporated and dried under high vacuum (oil pump). The compound
553 was purified by HPLC to yield ((*R*)-2-ammonio-3-azidopropanoyl)-D-alaninate 2,2,2-
554 trifluoroacetate (aDADA) as a white solid.

555 Frozen aliquots of a 500-mM stock solution of aDA-DA in 100% DMSO were diluted to 10 mM in
556 commercial DPBS (calcium- and magnesium-free, from ThermoFisher) and stored at -20°C for
557 subsequent use.

558 Powder of DBCO-AF647 (Jena Bioscience) was resuspended at 10 mM into 100% DMSO, diluted to
559 500 µM into DPBS and stored at -20°C for subsequent use.
560

561 **PG labeling in *S. pneumoniae* cells**

562 Cells in exponential growth phase (OD_{600nm} 0.3) were incubated for 5 min at 37°C in BHI medium
563 containing 2 mM aDA-DA (PULSE labeling). For PULSE-CHASE labeling experiments, after the 5-min
564 PULSE labeling with aDA-DA, cells were pelleted (7,000 × g, 5 min, 20°C) and resuspended into fresh,
565 pre-warmed BHI medium. Incubation at 37°C was continued for 15 min. Following PULSE or PULSE-
566 CHASE labeling, cells were fixed overnight on ice, in the culture medium supplemented with 0.5-X
567 DPBS and 2% (v/v) paraformaldehyde (PFA). Following fixation, cells were pelleted, resuspended
568 into DPBS containing 35 µM DBCO-AF647 and incubated for 1 h at 20°C (click reaction). Cells were
569 then washed twice with 1 mL of DPBS and were resuspended into the dSTORM buffer, which
570 contains 25 mM NaCl, 75 mM Tris-HCl pH 8.0, 10% (w/v) D-glucose, 100 mM cysteamine (β-
571 mercaptoethylamine) and 1X GLOX mix [40 $\mu g \cdot mL^{-1}$ catalase from bovine liver (Sigma-Aldrich), 0.5

572 mg·mL^{-1} glucose oxidase type VII from *Aspergillus niger* (Sigma-Aldrich)]. Further details regarding
573 the labeling procedure and alternative strategies can be found in (Trouve et al., 2021a).
574

575 **dSTORM data acquisition**

576 To perform dSTORM on cells oriented along their longitudinal axis, the samples were mounted
577 between a slide (High-precision, No. 1.5H, 24 X 50 mm, 170 ± 5 mm, Marienfeld) and a coverslip
578 (High-precision, No. 1.5H, 22 X 22 mm, 170 ± 5 µm, Marienfeld) previously treated with ozone and
579 eventually sealed with colorless nail polish.

580 To orient cells with a tilt angle, 8 µL of sample was loaded on a slide and covered with 18 µL of
581 dSTORM buffer containing 0.9% (w/v) low-melting agarose. The slide was then turned over onto a
582 coverslip. After solidification, the agarose pad was sealed with colorless nail polish.

583 dSTORM images were acquired at 27°C with a SAFe360 Abbelight PALM/STORM setup based on an
584 Olympus IX83 inverted microscope equipped with a Oxxius laser combiner and two sCMOS
585 Hamamatsu ORCA-Fusion cameras controlled via the NEO software. The emitted signal was
586 collected by a 100x oil immersion apochromatic objective (UPLAPO100XOHR, Olympus) and then
587 filtered by a band-pass filter FF01-698/70 (Semrock). First, diffraction-limited images were
588 acquired by illuminating the sample at 640 nm with 1% of the maximal laser power (2 kW·cm^{-2}).
589 For single-molecule localization microscopy, the samples were exposed to a continuous 640 nm
590 illumination with a constant laser power density of 2 kW·cm^{-2}. dSTORM data were collected over
591 15,000 frames recorded with an exposure time of 50 ms. The blinking density was maintained all
592 along the data collection by ramping up a 405-nm laser from 0% to 15% of a maximal value of 50
593 W·cm^{-2} For homogenous excitation of the sample, the field of excitation parameter in the NEO
594 software was adjusted to cover the region of interest (ASTER illumination) (Mau et al., 2021).
595

596 **dSTORM image reconstruction**

597 Data processing was performed with the ThunderSTORM plugin in ImageJ/FIJI (Ovesný et al., 2014;
598 Schindelin et al., 2012; Schneider et al., 2012), including determination of the localization precision
599 and quantification of the number of localizations. Potential drift was corrected with the cross-
600 correlation tool in ThunderSTORM (Ovesný et al., 2014). Image rendering was achieved through
601 normalized Gaussian blurring with a reconstructed pixel size of 10 nm. The spatial resolution of the
602 reconstructed dSTORM images was calculated using the FIRE ImageJ/FIJI plugin (Nieuwenhuizen et

al., 2013). Further details for dSTORM data acquisition and image reconstruction can be found in (Trouve et al., 2021a).

Measurement of the labeling patterns

Measurements of the labeled regions were performed in ImageJ (Schneider et al., 2012). The values of the diameter d and of the width of the chase W_{CHASE} (as defined in figures 2C and 5B) were obtained by plotting the signal intensity along a line positioned over the labeling of interest and measuring the distance between the points at half the maximal intensity.

For radial labeling patterns (in vertical or angled bacteria), the diameters d_{out} and d_{in} used to calculate the radial thickness r of the labeled region, as defined in figure 4B, were measured as above along a line positioned across the longest axis of the elliptic patterns.

Geometrical model of cell growth and labeling

The basis of the geometrical model was similar to that developed previously for WT strains (Trouve et al., 2021b). The animated geometrical model was implemented using the free open source 3D animation software Art of Illusion© by Peter Eastman. The mature cell was modeled as an ellipsoid of length L and diameter D. Taking the longitudinal axis as the x axis, the equator as its origin, and L the length of a mature single cell, the radius of the cell around this axis (R_{out}) is given by the elliptic curve:

$$R_{out_{(x)}} = \sqrt{y_{out}^2 + z_{out}^2} = \sqrt{1 - \left(\frac{x}{L/2}\right)^2}$$

Taking l as the distance between two parting equators, as the new cell length $l/2$ grows along x with time, R_{out} at $x = l/2$ is the radius of the septal outer edge circle ($R_{out} = d_{out}/2$). Taking the length C, at which the septum is closed, the radius of the septal inner edge circle ($R_{in} = d_{in}/2$) at $x = l/2$ is given by:

$$R_{in_{(x)}} = \sqrt{y_{in}^2 + z_{in}^2} = \sqrt{1 - \left(\frac{x}{C/2}\right)^2}$$

That points on the inner septal edge follow an elliptic path towards the point of closure is an assumption that was found to match the observations of the WT strains. We have set $R_{\max} = D/2 = 1$, so that in the above equations, $L/2$ takes the numerical value of the elliptic factor $E = L/D$.

To account for the acceleration of the growth along the x axis observed in WT strains, $l/2$ depends on time according to:

$$l/2_{(t)} = \frac{(1 + At)}{2(1 + A)}$$

where A is an acceleration factor. Note that in this equation, t and A are dimensionless and t is expressed as a fraction of the generation time, which is defined as 1. The (1+A) denominator is a normalization factor that ensures that a division is completed at t = 1.

Since the acceleration was not observed in the Δ*divIVA* strain, A was set to 0 to describe the deletion phenotype. Instead, three additional parameters were introduced in the model. A time point after the initiation of the division at which the cell elongation slows down (T_s), and the factor by which the elongation rate is diminished ("brake" factor B). When B is set to 1, growth continues unchanged after T_s at the normalized rate of 1 and the division cycle is completed at t = 1. If B is set as a fraction of 1, the cell elongation continues at rate B after T_s, and the division ends at $t = T_s + (1-T_s)/B$, which is greater than 1.

$$l/2_{(t<T_s)} =$$

$$l/2_{(t>T_s)} = LT_s + BL(t - T_s)$$

The third parameter that was added determines a point at which all processes stop. For practical reason of programming in Art of Illusion©, this event was defined as a fraction (S) of the length that the cell would have attained without growth arrest, rather than as a time.

The start and length of the labeling pulse can also be defined. In contrast to the WT strains, where the evolution of the various distances (length l, inner and outer septal diameter d_{in} and d_{out} could be fitted to measurements to extract values of the model parameters, the parameter describing the Δ*divIVA* strain were manually adjusted to best reproduce the observations, due to the greater heterogeneity of the cell sizes and morphologies. Nevertheless, all the simulated labeling patterns presented were generated with the same set of parameters, which are given in Table 1.

Quantification and Statistical Analysis

Statistics were performed using Excel and figures were prepared using LabPlot2. The statistical details describing the quantification and measurements of localization patterns (including the

definition of center, dispersion and precision of measures, the statistical tests used, the exact value of the *n* number of analyzed cells) can be found in the *Results* section and in the figure legends.

Materials and Data Availability

There are restrictions to the availability of the aDA-DA probe. Due to the time required for chemical synthesis, this material will be available through a collaboration with Yung-Sing Wong (yung-sing.wong@univ-grenoble-alpes.fr).

The datasets generated during this study will be made available on the Zenodo platform upon acceptation of the manuscript [accession # To be named/zenodo.org].

Acknowledgments

We thank members of the Morlot and Grangeasse laboratories for advice and encouragement, O. Glushonkov and J.P. Kleman for advices and support regarding dSTORM. Support for this work comes from the Agence Nationale de la Recherche (ANR-16-CE11-0016 and ANR-23-CE11-0029 to CM, ANR-19-CE15-0011 to CG, Labex ARCANE ANR-17-EURE-0003 to YSW, and ANR-17-CE13-0031 to RCL and NC). This work used the platforms of the Grenoble Instruct-ERIC centre (ISBG; UMS 3518 CNRS-CEA-UGA-EMBL) within the Grenoble Partnership for Structural Biology (PSB), supported by FRISBI (ANR-10-INBS-05-02) and GRAL, financed within the University Grenoble Alpes graduate school (Ecoles Universitaires de Recherche) CBH-EUR-GS (ANR-17-EURE-0003). IBS acknowledges integration into the Interdisciplinary Research Institute of Grenoble (IRIG, CEA).

Author contributions

JT, AZ, RCL, NC, YSW, CG and CM designed research; JT, AZ, LB, DJ, AP, CF and MB performed experiments; JT, AZ, DJ, NC, YSW, CG and CM analyzed data; JT, AZ and CM wrote the manuscript; JT, AZ, RCL, NC, YSW, CG and CM revised the manuscript.

Declaration of Interests

The authors declare no competing interests.

Inclusion and Diversity Statement

While citing references scientifically relevant for this work, we also actively worked to promote gender balance in our reference list.

References

Bai, X.-H., Chen, H.-J., Jiang, Y.-L., Wen, Z., Huang, Y., Cheng, W., Li, Q., Qi, L., Zhang, J.-R., Chen, Y., Zhou, C.-Z., 2014. Structure of pneumococcal peptidoglycan hydrolase LytB reveals insights into the bacterial cell wall remodeling and pathogenesis. J. Biol. Chem. 289, 23403–23416. https://doi.org/10.1074/jbc.M114.579714

Barendt, S.M., Land, A.D., Sham, L.-T., Ng, W.-L., Tsui, H.-C.T., Arnold, R.J., Winkler, M.E., 2009. Influences of Capsule on Cell Shape and Chain Formation of Wild-Type and pcsB Mutants of Serotype 2 Streptococcus pneumoniae. J. Bacteriol. 191, 3024–3040. https://doi.org/10.1128/JB.01505-08

Bartual, S.G., Straume, D., Stamsås, G.A., Muñoz, I.G., Alfonso, C., Martínez-Ripoll, M., Håvarstein, L.S., Hermoso, J.A., 2014. Structural basis of PcsB-mediated cell separation in Streptococcus pneumoniae. Nat. Commun. 5, 3842. https://doi.org/10.1038/ncomms4842

Berg, K.H., Stamsås, G.A., Straume, D., Håvarstein, L.S., 2013. Effects of Low PBP2b Levels on Cell Morphology and Peptidoglycan Composition in Streptococcus pneumoniae R6. J. Bacteriol. 195, 4342–4354. https://doi.org/10.1128/JB.00184-13

Billaudeau, C., Chastanet, A., Yao, Z., Cornilleau, C., Mirouze, N., Fromion, V., Carballido-López, R., 2017. Contrasting mechanisms of growth in two model rod-shaped bacteria. Nat. Commun. 8, 15370. https://doi.org/10.1038/ncomms15370

Briggs, N.S., Bruce, K.E., Naskar, S., Winkler, M.E., Roper, D.I., 2021. The Pneumococcal Divisome: Dynamic Control of Streptococcus pneumoniae Cell Division. Front. Microbiol. 12, 737396. https://doi.org/10.3389/fmicb.2021.737396

Cho, H., Wivagg, C.N., Kapoor, M., Barry, Z., Rohs, P.D.A., Suh, H., Marto, J.A., Garner, E.C., Bernhardt, T.G., 2016. Bacterial cell wall biogenesis is mediated by SEDS and PBP polymerase families functioning semi-autonomously. Nat. Microbiol. 16172. https://doi.org/10.1038/nmicrobiol.2016.172

726 Choukate, K., Chaudhuri, B., 2020. Structural basis of self-assembly in the lipid-binding domain of
727 mycobacterial polar growth factor Wag31. IUCrJ 7, 767–776.
728 https://doi.org/10.1107/S2052252520006053

729 Cramer, K., Reinhardt, S.C.M., Auer, A., Shin, J.Y., Jungmann, R., 2024. Comparing divisome organization
730 between vegetative and sporulating Bacillus subtilis at the nanoscale using DNA-PAINT. Sci. Adv. 10,
731 eadk5847. https://doi.org/10.1126/sciadv.adk5847

732 De Las Rivas, B., García, J.L., López, R., García, P., 2002. Purification and polar localization of pneumococcal
733 LytB, a putative endo-beta-N-acetylglucosaminidase: the chain-dispersing murein hydrolase. J. Bacteriol.
734 184, 4988–5000. https://doi.org/10.1128/JB.184.18.4988-5000.2002

735 Eswaramoorthy, P., Erb, M.L., Gregory, J.A., Silverman, J., Pogliano, K., Pogliano, J., Ramamurthi, K.S., 2011.
736 Cellular architecture mediates DivIVA ultrastructure and regulates min activity in Bacillus subtilis. mBio 2,
737 e00257-11. https://doi.org/10.1128/mBio.00257-11

738 Fadda, D., Pischedda, C., Caldara, F., Whalen, M.B., Anderluzzi, D., Domenici, E., Massidda, O., 2003.
739 Characterization of divIVA and Other Genes Located in the Chromosomal Region Downstream of the dcw
740 Cluster in Streptococcus pneumoniae. J. Bacteriol. 185, 6209–6214.
741 https://doi.org/10.1128/JB.185.20.6209-6214.2003

742 Fadda, D., Santona, A., D'Ulisse, V., Ghelardini, P., Ennas, M.G., Whalen, M.B., Massidda, O., 2007. Streptococcus
743 pneumoniae DivIVA: localization and interactions in a MinCD-free context. J. Bacteriol. 189, 1288–1298.
744 https://doi.org/10.1128/JB.01168-06

745 Fleurie, A., Manuse, S., Zhao, C., Campo, N., Cluzel, C., Lavergne, J.-P., Freton, C., Combet, C., Guiral, S., Soufi, B.,
746 Macek, B., Kuru, E., VanNieuwenhze, M.S., Brun, Y.V., Guilmi, A.-M.D., Claverys, J.-P., Galinier, A., Grangeasse,
747 C., 2014. Interplay of the Serine/Threonine-Kinase StkP and the Paralogs DivIVA and GpsB in
748 Pneumococcal Cell Elongation and Division. PLOS Genet 10, e1004275.
749 https://doi.org/10.1371/journal.pgen.1004275

750 Giacomelli, G., Feddersen, H., Peng, F., Martins, G.B., Grafemeyer, M., Meyer, F., Mayer, B., Graumann, P.L.,
751 Bramkamp, M., 2022. Subcellular Dynamics of a Conserved Bacterial Polar Scaffold Protein. Genes 13, 278.
752 https://doi.org/10.3390/genes13020278

753 Halbedel, S., Lewis, R.J., 2019. Structural basis for interaction of DivIVA/GpsB proteins with their ligands. Mol.
754 Microbiol. 111, 1404–1415. https://doi.org/10.1111/mmi.14244

755 Hammond, L.R., White, M.L., Eswara, P.J., 2019. ¡vIVA la DivIVA! J. Bacteriol. 201, e00245-19.
756 https://doi.org/10.1128/JB.00245-19

757 Jacq, M., Adam, V., Bourgeois, D., Moriscot, C., Guilmi, A.-M.D., Vernet, T., Morlot, C., 2015. Remodeling of the Z-
758 Ring Nanostructure during the Streptococcus pneumoniae Cell Cycle Revealed by Photoactivated
759 Localization Microscopy. mBio 6, pii: e01108-15. https://doi.org/10.1128/mBio.01108-15

760 Jacq, M., Arthaud, C., Manuse, S., Mercy, C., Bellard, L., Peters, K., Gallet, B., Galindo, J., Doan, T., Vollmer, W.,
761 Brun, Y.V., VanNieuwenhze, M.S., Guilmi, A.M.D., Vernet, T., Grangeasse, C., Morlot, C., 2018. The cell wall
762 hydrolase Pmp23 is important for assembly and stability of the division ring in Streptococcus
763 pneumoniae. Sci. Rep. 8, 7591. https://doi.org/10.1038/s41598-018-25882-y

764 Jiang, Q., Li, B., Zhang, L., Li, T., Hu, Q., Li, H., Zou, W., Hu, Z., Huang, Q., Zhou, R., 2023. DivIVA Interacts with the
765 Cell Wall Hydrolase MltG To Regulate Peptidoglycan Synthesis in Streptococcus suis. Microbiol. Spectr. 11,
766 e0475022. https://doi.org/10.1128/spectrum.04750-22

767 Juillot, D., Billaudeau, C., Barbotin, A., Lablaine, A., Mortier-Barrière, I., Polard, P., Campo, N., Carballido-Lopez,
768 R., 2024. Transient inhibition of cell division in competent pneumococcal cells results from deceleration of
769 the septal peptidoglycan complex (preprint). Microbiology. https://doi.org/10.1101/2024.02.28.582556

770 Kang, C.-M., Nyayapathy, S., Lee, J.-Y., Suh, J.-W., Husson, R.N., 2008. Wag31, a homologue of the cell division
771 protein DivIVA, regulates growth, morphology and polar cell wall synthesis in mycobacteria. Microbiol.
772 Read. Engl. 154, 725–735. https://doi.org/10.1099/mic.0.2007/014076-0

773 Käshammer, L., van den Ent, F., Jeffery, M., Jean, N.L., Hale, V.L., Löwe, J., 2023. Cryo-EM structure of the
774 bacterial divisome core complex and antibiotic target FtsWIQBL. Nat. Microbiol.
775 https://doi.org/10.1038/s41564-023-01368-0

Letek, M., Ordóñez, E., Vaquera, J., Margolin, W., Flärdh, K., Mateos, L.M., Gil, J.A., 2008. DivIVA is required for polar growth in the MreB-lacking rod-shaped actinomycete Corynebacterium glutamicum. J. Bacteriol. 190, 3283–3292. https://doi.org/10.1128/JB.01934-07

Liechti, G.W., Kuru, E., Hall, E., Kalinda, A., Brun, Y.V., VanNieuwenhze, M., Maurelli, A.T., 2014. A new metabolic cell-wall labelling method reveals peptidoglycan in *Chlamydia trachomatis* . Nature 506, 507–510. https://doi.org/10.1038/nature12892

Mau, A., Friedl, K., Leterrier, C., Bourg, N., Lévêque-Fort, S., 2021. Fast widefield scan provides tunable and uniform illumination optimizing super-resolution microscopy on large fields. Nat. Commun. 12, 3077. https://doi.org/10.1038/s41467-021-23405-4

McAllister, T.E., Nix, M.G., Webb, M.E., 2011. Fmoc-chemistry of a stable phosphohistidine analogue. Chem. Commun. Camb. Engl. 47, 1297–1299. https://doi.org/10.1039/c0cc04238b

Meeske, A.J., Riley, E.P., Robins, W.P., Uehara, T., Mekalanos, J.J., Kahne, D., Walker, S., Kruse, A.C., Bernhardt, T.G., Rudner, D.Z., 2016. SEDS proteins are a widespread family of bacterial cell wall polymerases. Nature 537, 634–638. https://doi.org/10.1038/nature19331

Nieuwenhuizen, R.P.J., Lidke, K.A., Bates, M., Puig, D.L., Grünwald, D., Stallinga, S., Rieger, B., 2013. Measuring image resolution in optical nanoscopy. Nat. Methods 10, 557–562. https://doi.org/10.1038/nmeth.2448

Oliva, M.A., Halbedel, S., Freund, S.M., Dutow, P., Leonard, T.A., Veprintsev, D.B., Hamoen, L.W., Löwe, J., 2010. Features critical for membrane binding revealed by DivIVA crystal structure. EMBO J. 29, 1988–2001. https://doi.org/10.1038/emboj.2010.99

Ovesný, M., Křížek, P., Borkovec, J., Svindrych, Z., Hagen, G.M., 2014. ThunderSTORM: a comprehensive ImageJ plug-in for PALM and STORM data analysis and super-resolution imaging. Bioinforma. Oxf. Engl. 30, 2389–2390. https://doi.org/10.1093/bioinformatics/btu202

Paik, J., Kern, I., Lurz, R., Hakenbeck, R., 1999. Mutational analysis of the Streptococcus pneumoniae bimodular class A penicillin-binding proteins. J. Bacteriol. 181, 3852–3856. https://doi.org/10.1128/JB.181.12.3852-3856.1999

Perez, A.J., Boersma, M.J., Bruce, K.E., Lamanna, M.M., Shaw, S.L., Tsui, H.-C.T., Taguchi, A., Carlson, E.E., VanNieuwenhze, M.S., Winkler, M.E., 2021. Organization of peptidoglycan synthesis in nodes and separate rings at different stages of cell division of Streptococcus pneumoniae. Mol. Microbiol. 115, 1152–1169. https://doi.org/10.1111/mmi.14659

Perez, A.J., Cesbron, Y., Shaw, S.L., Bazan Villicana, J., Tsui, H.-C.T., Boersma, M.J., Ye, Z.A., Tovpeko, Y., Dekker, C., Holden, S., Winkler, M.E., 2019. Movement dynamics of divisome proteins and PBP2x:FtsW in cells of Streptococcus pneumoniae. Proc. Natl. Acad. Sci. U. S. A. 116, 3211–3220. https://doi.org/10.1073/pnas.1816018116

Philippe, J., Vernet, T., Zapun, A., 2014. The Elongation of Ovococci. Microb. Drug Resist. 20, 215–221. https://doi.org/10.1089/mdr.2014.0032

Pinho, M.G., Kjos, M., Veening, J.-W., 2013. How to get (a)round: mechanisms controlling growth and division of coccoid bacteria. Nat. Rev. Microbiol. 11, 601–614. https://doi.org/10.1038/nrmicro3088

Reichmann, N.T., Tavares, A.C., Saraiva, B.M., Jousselin, A., Reed, P., Pereira, A.R., Monteiro, J.M., Sobral, R.G., VanNieuwenhze, M.S., Fernandes, F., Pinho, M.G., 2019. SEDS-bPBP pairs direct lateral and septal peptidoglycan synthesis in Staphylococcus aureus. Nat. Microbiol. 4, 1368–1377. https://doi.org/10.1038/s41564-019-0437-2

Sauvage, E., Kerff, F., Terrak, M., Ayala, J.A., Charlier, P., 2008. The penicillin-binding proteins: structure and role in peptidoglycan biosynthesis. FEMS Microbiol. Rev. 32, 234–258. https://doi.org/10.1111/j.1574-6976.2008.00105.x

Schermelleh, L., Ferrand, A., Huser, T., Eggeling, C., Sauer, M., Biehlmaier, O., Drummen, G.P.C., 2019. Super-resolution microscopy demystified. Nat. Cell Biol. 21, 72–84. https://doi.org/10.1038/s41556-018-0251-8

Schindelin, J., Arganda-Carreras, I., Frise, E., Kaynig, V., Longair, M., Pietzsch, T., Preibisch, S., Rueden, C., Saalfeld, S., Schmid, B., Tinevez, J.-Y., White, D.J., Hartenstein, V., Eliceiri, K., Tomancak, P., Cardona, A., 2012. Fiji: an open-source platform for biological-image analysis. Nat. Methods 9, 676–682. https://doi.org/10.1038/nmeth.2019

827 Schneider, C.A., Rasband, W.S., Eliceiri, K.W., 2012. NIH Image to ImageJ: 25 years of image analysis. Nat.
828 Methods 9, 671–675. https://doi.org/10.1038/nmeth.2089

829 Sjodt, M., Rohs, P.D.A., Gilman, M.S.A., Erlandson, S.C., Zheng, S., Green, A.G., Brock, K.P., Taguchi, A., Kahne, D.,
830 Walker, S., Marks, D.S., Rudner, D.Z., Bernhardt, T.G., Kruse, A.C., 2020. Structural coordination of
831 polymerization and crosslinking by a SEDS-bPBP peptidoglycan synthase complex. Nat. Microbiol. 5, 813–
832 820. https://doi.org/10.1038/s41564-020-0687-z

833 Straume, D., Piechowiak, K.W., Kjos, M., Håvarstein, L.S., 2021. Class A PBPs: It is time to rethink traditional
834 paradigms. Mol. Microbiol. 116, 41–52. https://doi.org/10.1111/mmi.14714

835 Straume, D., Piechowiak, K.W., Olsen, S., Stamsås, G.A., Berg, K.H., Kjos, M., Heggenhougen, M.V., Alcorlo, M.,
836 Hermoso, J.A., Håvarstein, L.S., 2020. Class A PBPs have a distinct and unique role in the construction of
837 the pneumococcal cell wall. Proc. Natl. Acad. Sci. U. S. A. 117, 6129–6138.
838 https://doi.org/10.1073/pnas.1917820117

839 Straume, D., Stamsås, G.A., Berg, K.H., Salehian, Z., Håvarstein, L.S., 2017. Identification of pneumococcal
840 proteins that are functionally linked to penicillin-binding protein 2b (PBP2b). Mol. Microbiol. 103, 99–116.
841 https://doi.org/10.1111/mmi.13543

842 Sutton, J.A.F., Cooke, M., Tinajero-Trejo, M., Wacnik, K., Salamaga, B., Portman-Ross, C., Lund, V.A., Hobbs, J.K.,
843 Foster, S.J., 2023. The roles of GpsB and DivIVA in Staphylococcus aureus growth and division. Front.
844 Microbiol. 14, 1241249. https://doi.org/10.3389/fmicb.2023.1241249

845 Taguchi, A., Page, J.E., Tsui, H.-C.T., Winkler, M.E., Walker, S., 2021. Biochemical reconstitution defines new
846 functions for membrane-bound glycosidases in assembly of the bacterial cell wall. Proc. Natl. Acad. Sci. U.
847 S. A. 118, e2103740118. https://doi.org/10.1073/pnas.2103740118

848 Taguchi, A., Welsh, M.A., Marmont, L.S., Lee, W., Sjodt, M., Kruse, A.C., Kahne, D., Bernhardt, T.G., Walker, S.,
849 2019. FtsW is a peptidoglycan polymerase that is functional only in complex with its cognate penicillin-
850 binding protein. Nat. Microbiol. 4, 587–594. https://doi.org/10.1038/s41564-018-0345-x

851 Trouve, J., Glushonkov, O., Morlot, C., 2021a. Metabolic biorthogonal labeling and dSTORM imaging of
852 peptidoglycan synthesis in Streptococcus pneumoniae. STAR Protoc. 2, 101006.
853 https://doi.org/10.1016/j.xpro.2021.101006

854 Trouve, J., Zapun, A., Arthaud, C., Durmort, C., Di Guilmi, A.M., Söderström, B., Pelletier, A., Grangeasse, C.,
855 Bourgeois, D., Wong, Y.-S., Morlot, C., 2021b. Nanoscale dynamics of peptidoglycan assembly during the
856 cell cycle of Streptococcus pneumoniae. Curr. Biol. CB 31, 2844-2856.e6.
857 https://doi.org/10.1016/j.cub.2021.04.041

858 Tsui, H.-C.T., Zheng, J.J., Magallon, A.N., Ryan, J.D., Yunck, R., Rued, B.E., Bernhardt, T.G., Winkler, M.E., 2016.
859 Suppression of a deletion mutation in the gene encoding essential PBP2b reveals a new lytic
860 transglycosylase involved in peripheral peptidoglycan synthesis in Streptococcus pneumoniae D39. Mol.
861 Microbiol. 100, 1039–1065. https://doi.org/10.1111/mmi.13366

862 Vigouroux, A., Cordier, B., Aristov, A., Alvarez, L., Özbaykal, G., Chaze, T., Oldewurtel, E.R., Matondo, M., Cava,
863 F., Bikard, D., van Teeffelen, S., 2020. Class-A penicillin binding proteins do not contribute to cell shape but
864 repair cell-wall defects. eLife 9, e51998. https://doi.org/10.7554/eLife.51998

865 Vollmer, W., Blanot, D., Pedro, M.A.D., 2008a. Peptidoglycan structure and architecture. FEMS Microbiol. Rev.
866 32, 149–167. https://doi.org/10.1111/j.1574-6976.2007.00094.x

867 Vollmer, W., Joris, B., Charlier, P., Foster, S., 2008b. Bacterial peptidoglycan (murein) hydrolases. FEMS
868 Microbiol. Rev. 32, 259–286. https://doi.org/10.1111/j.1574-6976.2007.00099.x

869 Vollmer, W., Massidda, O., Tomasz, A., 2019. The Cell Wall of Streptococcus pneumoniae. Microbiol. Spectr. 7.
870 https://doi.org/10.1128/microbiolspec.GPP3-0018-2018

871 Zapun, A., Noirclerc-Savoye, M., Helassa, N., Vernet, T., 2012. Peptidoglycan Assembly Machines: The
872 Biochemical Evidence. Microb. Drug Resist. 18, 256–260. https://doi.org/10.1089/mdr.2011.0236

873 Zapun, A., Vernet, T., Pinho, M.G., 2008. The different shapes of cocci. FEMS Microbiol. Rev. 32, 345–360.
874 https://doi.org/10.1111/j.1574-6976.2007.00098.x

875

876

FIGURES AND FIGURE LEGENDS

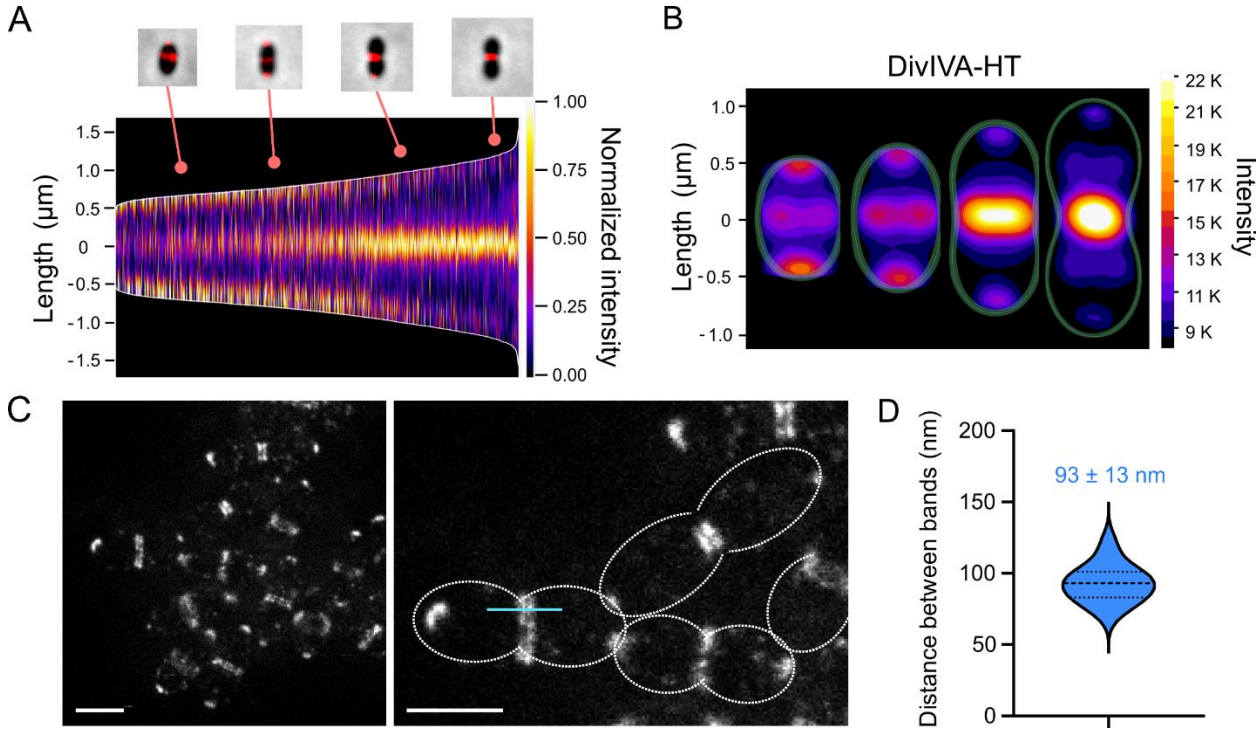

Figure 1. DivIVA localizes on both sides of constricting division sites in *S. pneumoniae*. Cells in exponential growth phase were incubated with HT-JFX646 ligand before fluorescence microcopy observation. **A.** Demograph showing the fluorescence intensity and diffraction-limited localization pattern of a DivIVA-HT fusion in 2,510 cells arranged according to their length. **B.** Heatmaps built from the localization patterns shown in (A) (n = 2,510), representing the average DivIVA-HT fluorescence intensity and localization along the cell cycle. Representative data are shown from two independent biological replicates. **C.** STED image showing the localization of DivIVA-HT as polar foci or as two bands flanking the division site. On the right panel, the cell contour is delineated with a dashed line and the blue line indicates a typical region used to generate intensity plot profiles. Scale bars, 1 µm. **D.** Violin plot showing the distribution of the distances separating DivIVA bands at midcell. The thin and thick dashed horizontal lines represent the quartiles (25th = 83 nm; 75th = 101 nm) and the median (93 nm) of two independent experiments, respectively. The median distance (n = 14) is indicated.

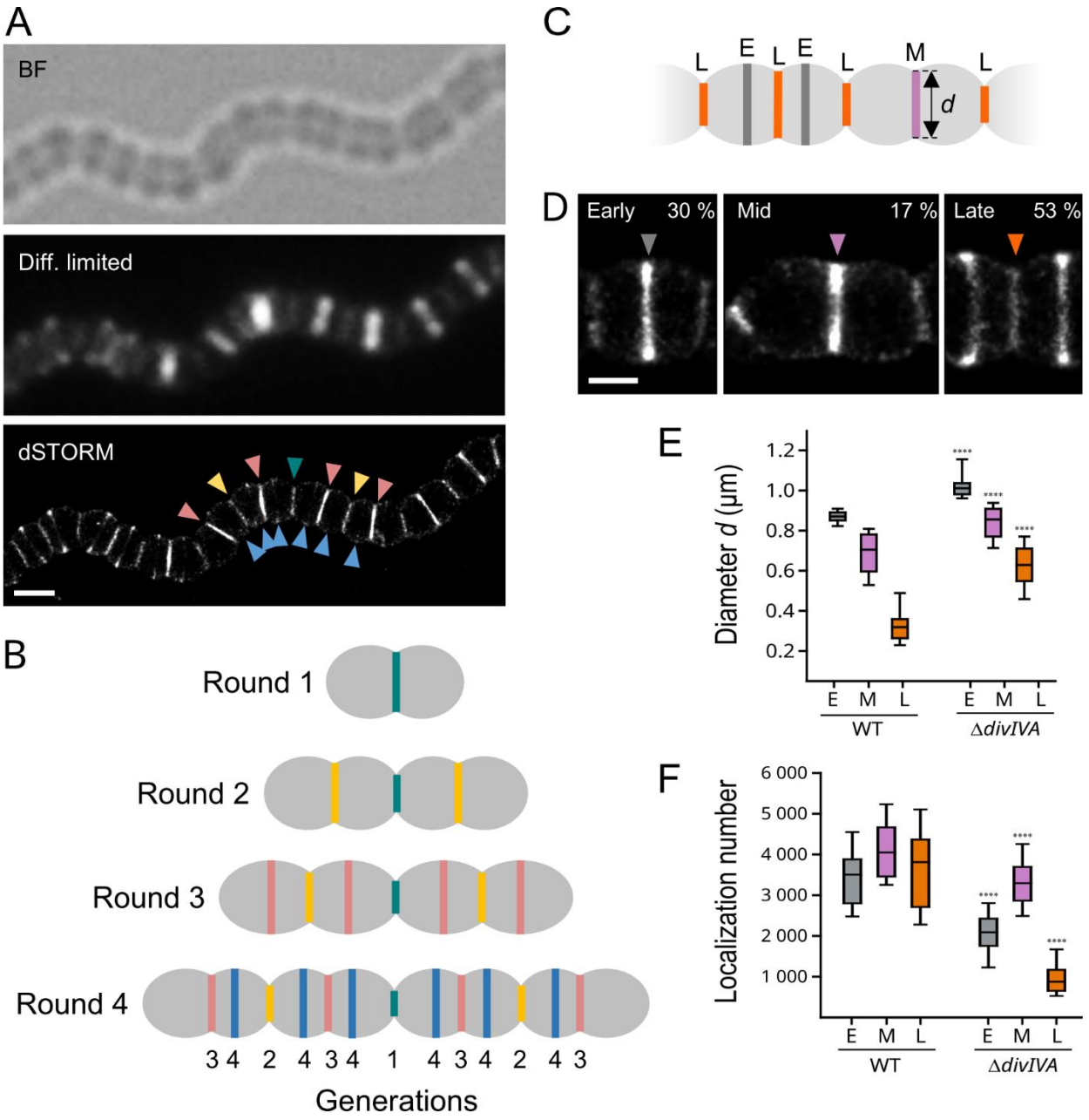

Figure 2. dSTORM analysis of PG synthesis in Δ*divIVA* cells. A. *S. pneumoniae* Δ*divIVA* cells in exponential growth phase were grown for 5 min in the presence of 2 mM aDA-DA, fixed and incubated with 35 µM DIBO-AF647 for fluorescent labeling. Bright field (BF), fluorescence diffraction-limited (Diff. limited) and reconstructed dSTORM images are shown. The arrowheads point to division sites of different generations, with a color code identical to that of panel B. Scale bar, 500 nm. **B.** Schematic illustration of the successive generations observed in Δ*divIVA* cell chains. **C.** Schematic diagram of pulse-labeled Δ*divIVA* cells lying along their longitudinal axis. The dark grey, purple and orange bands correspond respectively to early- (E), mid- (M) and late-

925 division (L) pulse-labeling patterns, defined by their respective diameter (*d*). **D.** Zoom on
926 representative dSTORM images of Δ*divIVA* cells displaying early-, mid- and late-division pulse-
927 labeling patterns. Scale bar, 250 nm. **E.** Distribution of the diameters *d* among early- (*E*), mid- (*M*)
928 and late-division (*L*) pulse-labeling patterns in wild-type (WT) (n = 116) and Δ*divIVA* (n = 200) cell
929 populations. **F.** Distribution of the number of localizations among early- (*E*), mid- (*M*) and late-
930 division (*L*) pulse-labeling patterns in wild-type (WT) (n = 116) and Δ*divIVA* (n = 200) cell
931 populations. **E-F.** Data are represented with box plots showing the interquartile range (10th and
932 90th percentile), the median value and whiskers for minimum and maximum values. P-values from
933 the U test of Mann-Whitney between WT and Δ*divIVA* data sets are indicated with quadruple
934 asterisks when the observed difference is statistically significant (p-value < 0.0001).

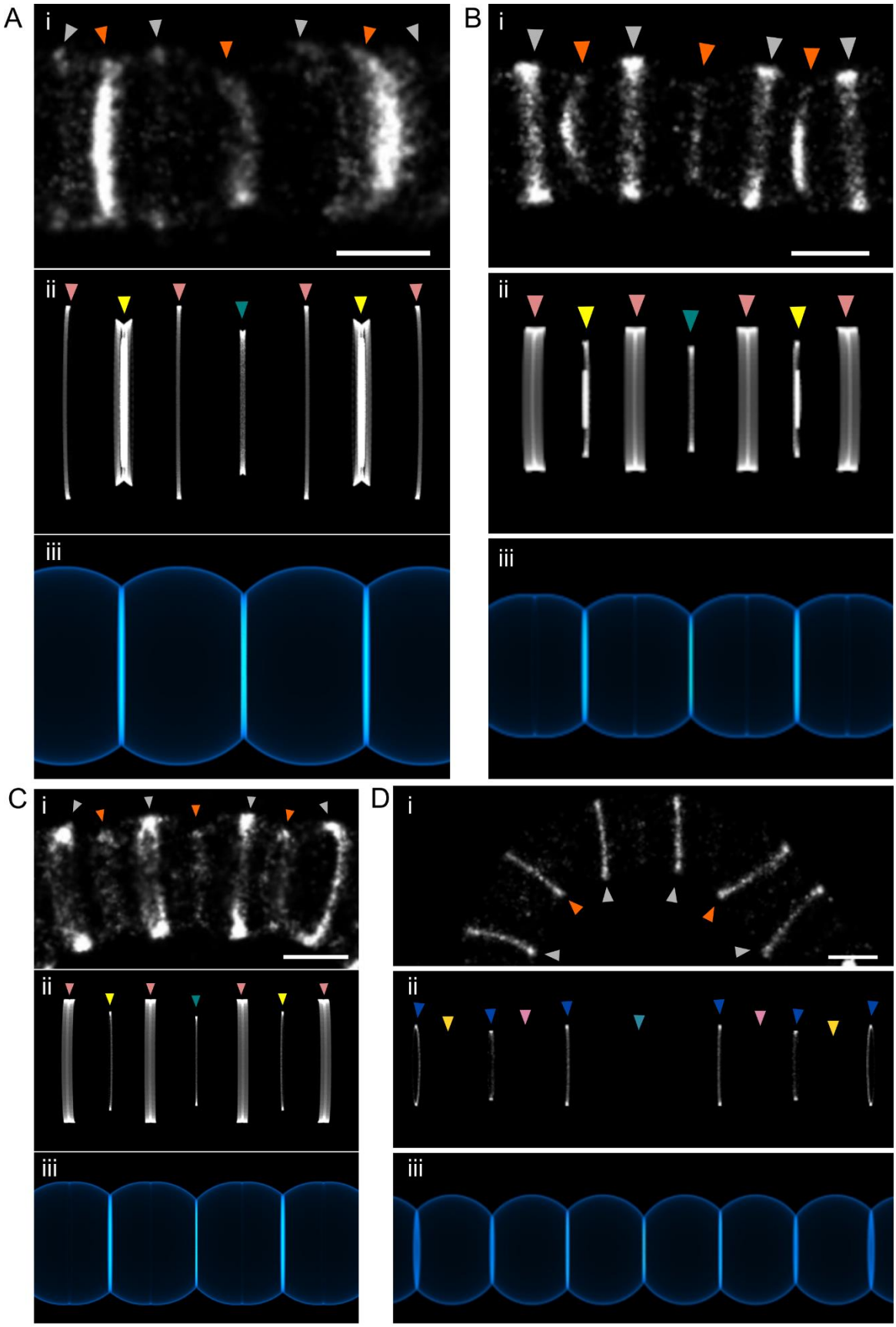

935

936 **Figure 3. Symmetrical banding patterns are reproduced by a dynamic geometrical model of**
937 **cell wall growth.** *S. pneumoniae* Δ*divIVA* cells in exponential growth phase were grown for 15 min
938 (**A** and **B**) or 5 min (**C** and **D**) in the presence of 2 mM aDA-DA, fixed and incubated with 35 μM
939 DIBO-AF647 for fluorescent labeling. Reconstructed dSTORM (i), simulated labeling patterns (ii)
940 and corresponding simulated cell wall (iii) images are shown. Scale bars, 500 nm. The same model
941 parameters given in Table 1 were used for all the patterns, while the timing and duration of the
942 labeling pulse were changed to generate each pattern (see Fig. S3).

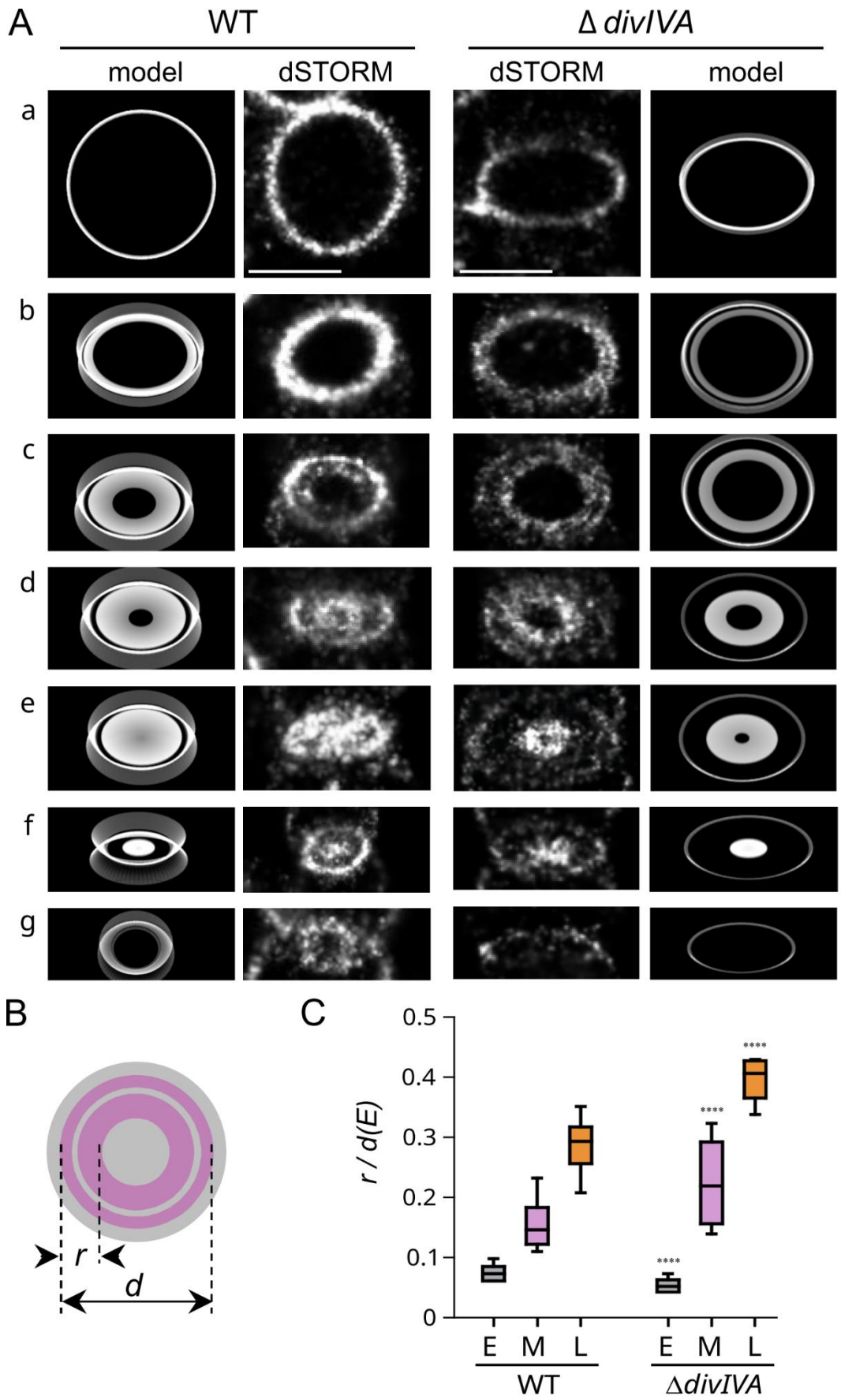
A
WT
Δ divIVA
model
dSTORM
dSTORM
model
a
b
c
d
e
f
g
B
r
d
C
r / d(E)
0.5
0.4
0.3
0.2
0.1
0
****
E
M
L
E
M
L
WT
ΔdivIVA

944 **Figure 4. PG synthesis observed in tilted cells.** **A**. Typical dSTORM localization patterns of
945 pulse-labeled PG in cells oriented vertically or at an angle in an agarose pad. Early- to late-division
946 stages are shown from top to bottom panels (*a*-*g*). Exponentially growing wild-type (WT) and
947 Δ*divIVA* cells were incubated for 5 min with aDA-DA, fixed, and labeled with DIBO-AF647 before
948 being trapped below an agarose pad. Scale bars, 500 nm. **B.** Schematic diagram representing a
949 mid-division cell oriented perpendicular to its longitudinal axis. This orientation allows observing
950 the septal (inner ring) and peripheral (outer ring) PG synthesis sites and measuring the radial
951 width (*r*) of the labeled region. **C.** Distribution of the radial width of labeling *r*, normalized to the
952 median largest diameter *d(E*) in early- (E), mid- (M) and late-division (L) pulse-labeling patterns in
953 WT (n = 170) and Δ*divIVA* (n = 149) cell populations. Data are represented with box plots showing
954 the interquartile range (10th and 90th percentile), the median value and whiskers for minimum and
955 maximum values. The quadruple asterisks represent a statistically significant difference between
956 WT and Δ*divIVA* datasets (U test of Mann-Whitney, p-value < 0.0001).

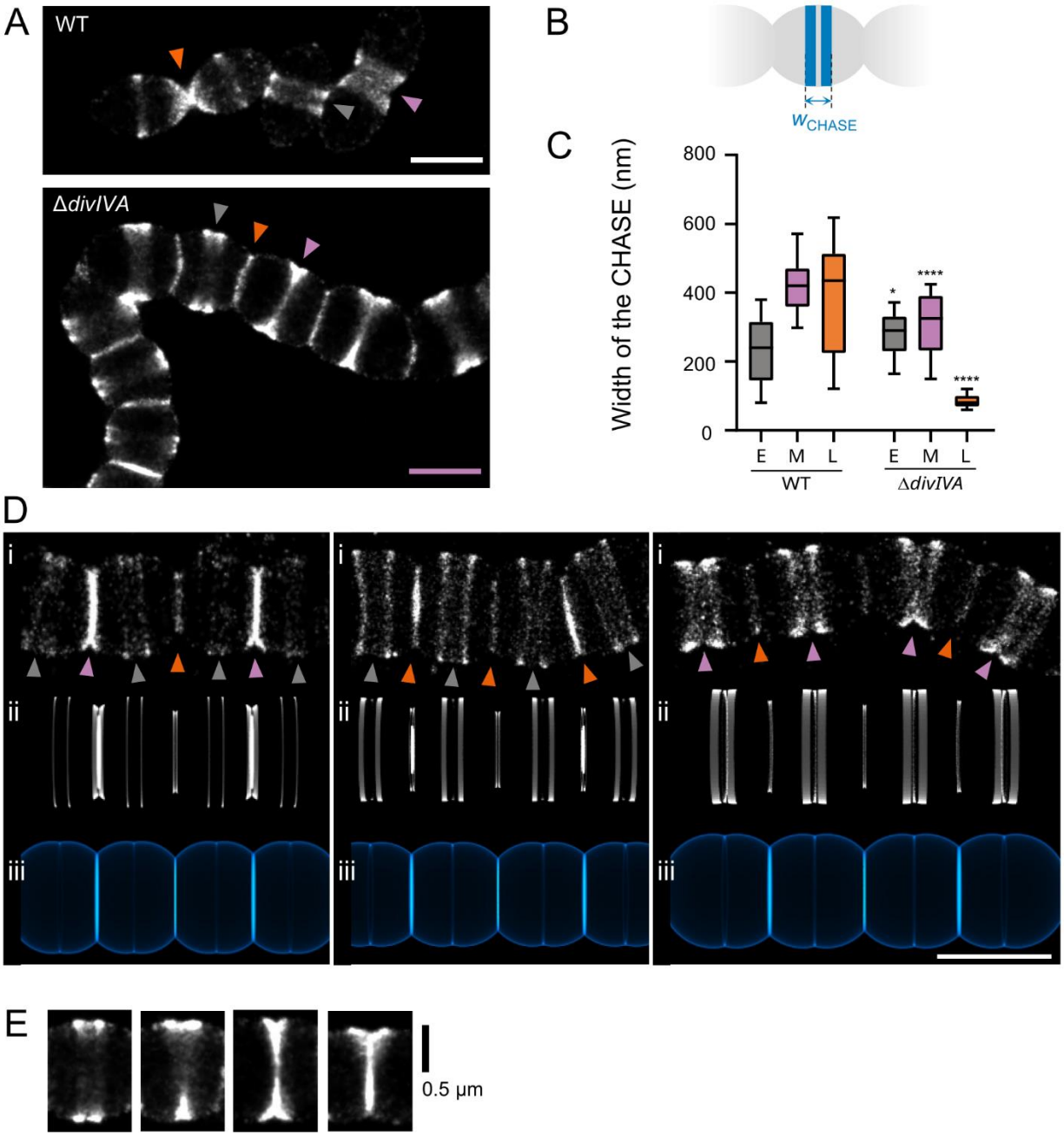

957

958 **Figure 5. Pulse-chase labeling patterns of Δ*divIVA* cells. A.** Representative dSTORM images of
959 pulse-chase localization patterns in wild-type and Δ*divIVA* cells. Exponentially growing cells were
960 incubated for 5 min with aDA-DA (pulse), grown for 15 min in the absence of the probe (chase),
961 fixed, and labeled with DIBO-AF647 before dSTORM data collection. The grey, violet and orange
962 arrowheads point to early-, mid- and late-division sites, respectively. Scale bars, 1 µm. **B.**
963 Schematic representation of a pulse-chase labeled cell harboring two bands at an early-division site.
964 The distance (W_{CHASE}) separating the longitudinal outer limits of the labeling pattern is shown. **C.**

965 Distributions of the W_{CHASE} of the labeling patterns in early- (E), mid- (M) and late-division (L) sites
966 (WT, n(*E*) = 89, n(M) = 68 and n(L) = 12; Δ*divIVA*, n(E) = 43, n(M) = 34 cells and n(L) = 101). Data
967 are represented with box plots showing the interquartile range (10th and 90th percentile), the
968 median value and whiskers for minimum and maximum values. P-values from the U test of Mann-
969 Whitney between different data sets are indicated with single or quadruple asterisks when the
970 observed differences are statistically significant with p-values < 0.01 or < 0.0001, respectively. **D.**
971 Typical symmetrical dSTORM localization patterns of pulse-chase labeled PG in Δ*divIVA* cells.
972 Earlier to later division stages are shown from left to right panels. Panels (i), (ii) and (iii) are
973 dSTORM images, simulations of the labeling patterns and corresponding cell wall, respectively.
974 Scale bar, 1 μm. **E.** dSTORM images of asymmetrical pulse-chase labeling patterns found with
975 Δ*divIVA* cells.

976

977

978

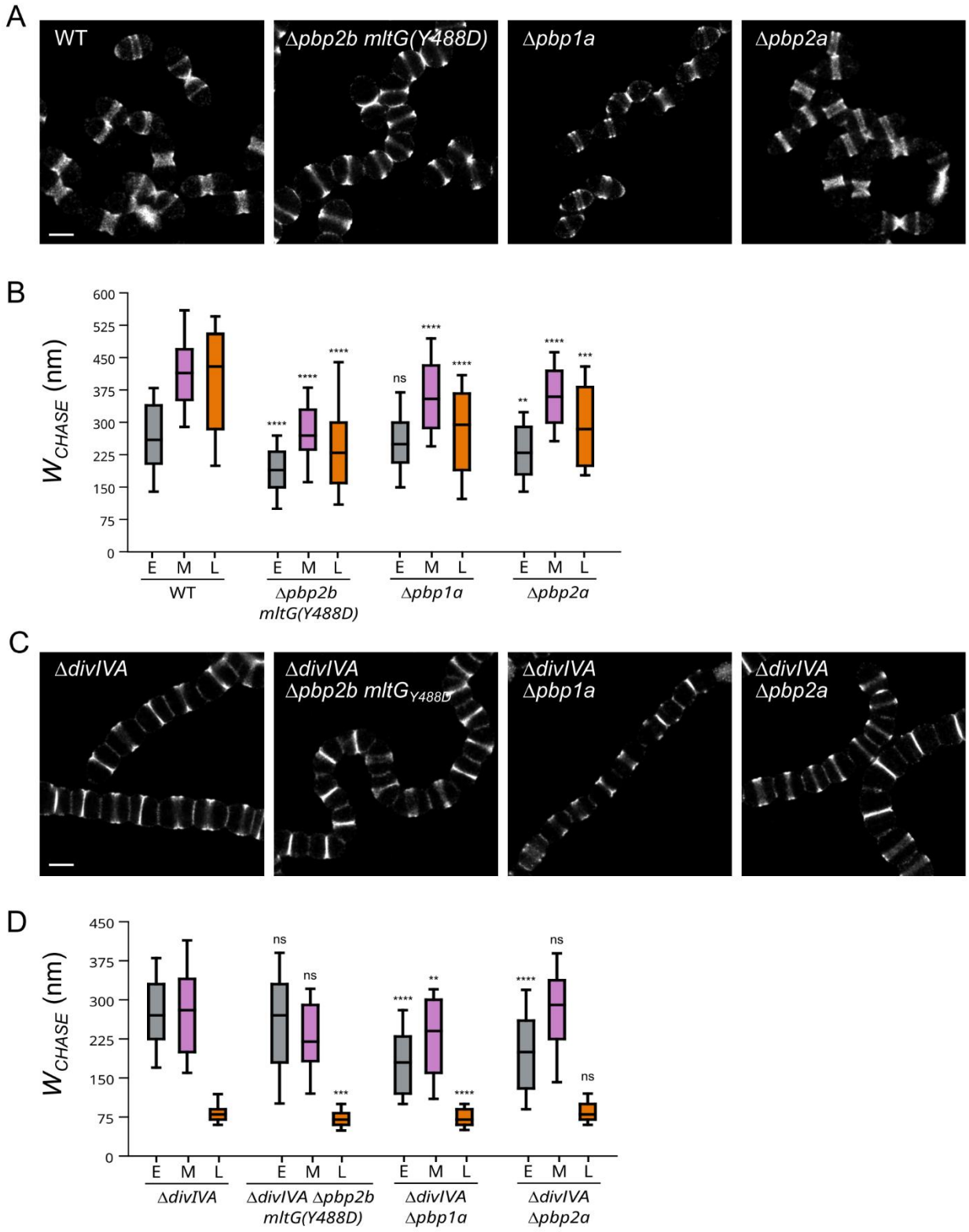

Figure 6. Effect of *pbp* gene deletion on Δ*divIVA* pulse-chase labeling patterns. A. Fields of wild-type (WT), Δ*pbp2b mltG(Y488D)*, Δ*pbp1a* and Δ*pbp2a* cells treated with the pulse-chase

982 labeling protocol and observed by dSTORM. Scale bar, 1 µm. **B.** Distributions of W_{CHASE} of the pulse-
983 chase labeling patterns observed in panel A (WT, n(E) = 132, n(M) = 123 and n(L) = 46; Δ*pbp2b*
984 *mltG*(Y488D), n(E) = 148, n(M) = 84 and n(L) = 65 cells; Δ*pbp1a*, n(E) = 140, n(M) = 116 and n(L) =
985 42 cells; Δ*pbp2a*, n(E) = 109, n(M) = 108 and n(L) = 40 cells). **C.** Fields of Δ*divIVA* mutant strains
986 cells treated with the pulse-chase labeling protocol and observed by dSTORM. Scale bar, 1 µm. **D.**
987 Distributions of W_{CHASE} of the pulse-chase labeling patterns observed in panel C (Δ*divIVA*, n(E) = 120,
988 n(M) = 57 and n(L) = 172 cells; Δ*divIVA* Δ*pbp2b mltG(Y488D)*, n(E) = 132, n(M) = 50 and n(L) = 120
989 cells; Δ*divIVA* Δ*pbp1a*, n(E) = 121, n(M) = 71 and n(L) = 109 cells; Δ*divIVA* Δ*pbp2a*, n(E) = 112, n(M)
990 = 42 and n(L) = 146 cells). **B** and **D**. Data are represented with box plots showing the interquartile
991 range (10th and 90th percentile), the median value and whiskers for minimum and maximum values.
992 P-values from the U test of Mann-Whitney between different data sets are indicated with double
993 asterisks when p-values < 0.01, triple asterisks when p-value < 0.001, quadruple asterisks when p-
994 values < 0.0001, or with "ns" when no significant difference is observed (p-value > 0.05).

995

996

997

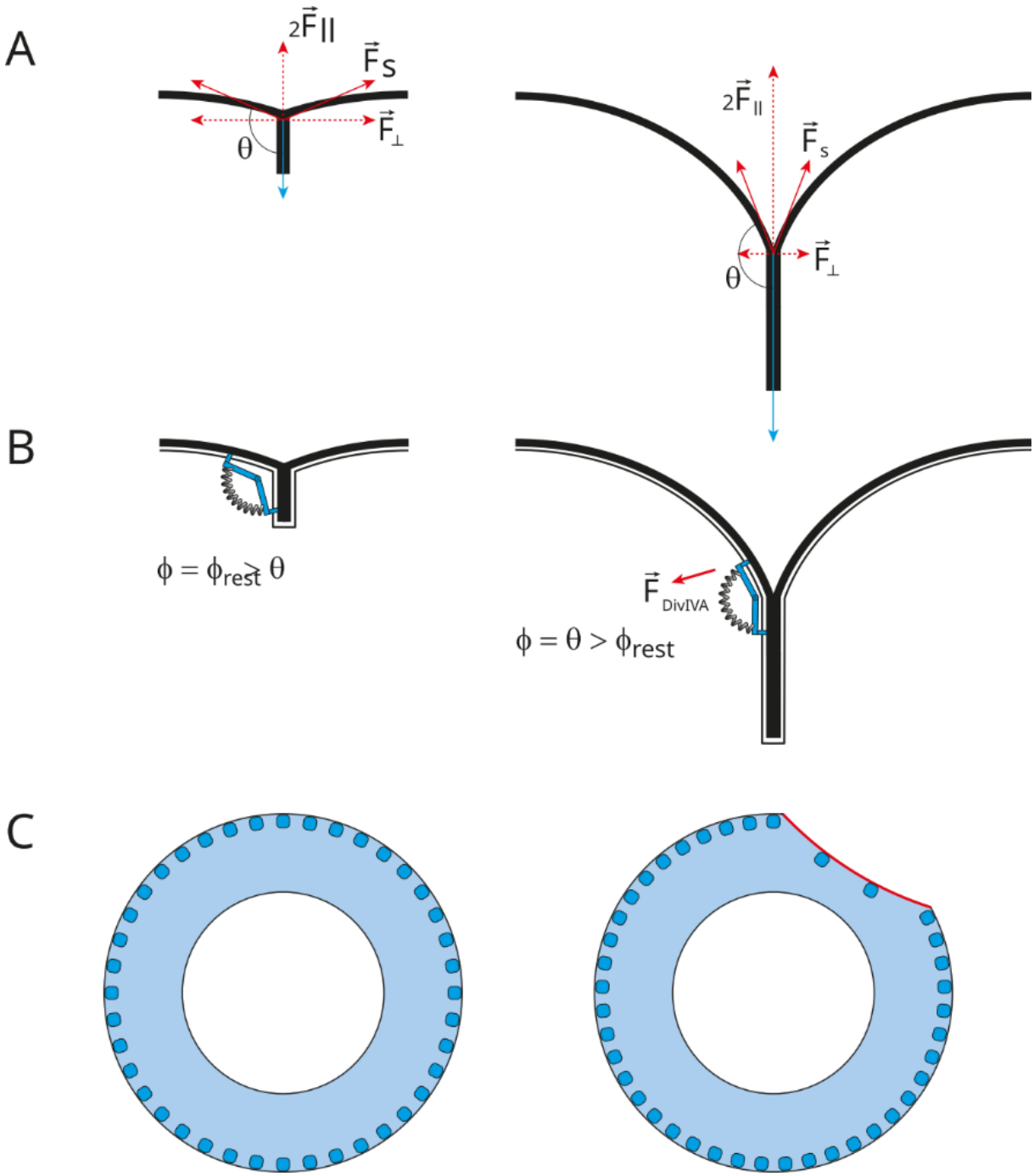

Figure 7. Model for the role of DivIVA in maintaining homogenous septum remodeling and peripheral PG synthesis in space and time. A. Schematic representation of the division site, with θ being the angle between the septal and peripheral walls and $|\vec{F}_s|$ the tangential force exerted by the turgor pressure at the site of septum cleavage. Taking the septal plane as a reference, $|\vec{F}_s|$ can be decomposed in a parallel ($|\vec{F}_{||}| = \cos\theta|\vec{F}_s|$) and a perpendicular ($|\vec{F}_{\perp}| = \sin\theta|\vec{F}_s|$) component. $\vec{F}_{\perp}$, which contributes to septal PG cleavage, and decreases as the septum splits to generate new

1005 hemispheres. **B.** In virtue of its polymeric nature and affinity for negatively curved membranes,
1006 DivIVA might display a conformation of minimal energy defined by a resting angle (ϕ_{rest}). Once ϕ_{rest}
1007 becomes smaller than θ, DivIVA stretching would generate a force that compensates the vanishing
1008 of the $\vec{F}_{\perp}$ force, or activates the septum remodeling machinery. **C.** Schematic representation of how
1009 negative curvature affinity of DivIVA (blue dots) could ensure uniform progression of splitting and
1010 peripheral synthesis around the septum (blue ring). If splitting/peripheral synthesis occurs along
1011 one section of the septum (red), the membrane curvature along this section decreases, leading to a
1012 reduced concentration of DivIVA. The reduced amount of DivIVA would slow down the
1013 splitting/synthesis in this region in comparison to the rest of the periphery, thus restoring a
1014 uniform progression around the division site
1015
1016
1017
1018 **Table 1**. Parameters of the geometrical model used simulate the cell wall growth.

strain		WT[a]	Δ*divIVA*
Diameter	D (μm)	0.85	0.98
Length	L (μm)	1.05	0.91
Elliptic ratio	$E = L/D$	1.24	0.93
Start of next generation as a fraction of the generation time	N	0.9	0.68
Acceleration factor	A	0.9	0
Septum closure as a fraction of generation time	C	0.84	0.68
Time of slowing elongation as a fraction of generation time	T_S	n/a	0.58
"Brake" factor	B	n/a	0.13
Fraction of complete length at which all processes stop	S	n/a	0.8

1019 [a] Reported from (Trouve et al., 2021b).
1020

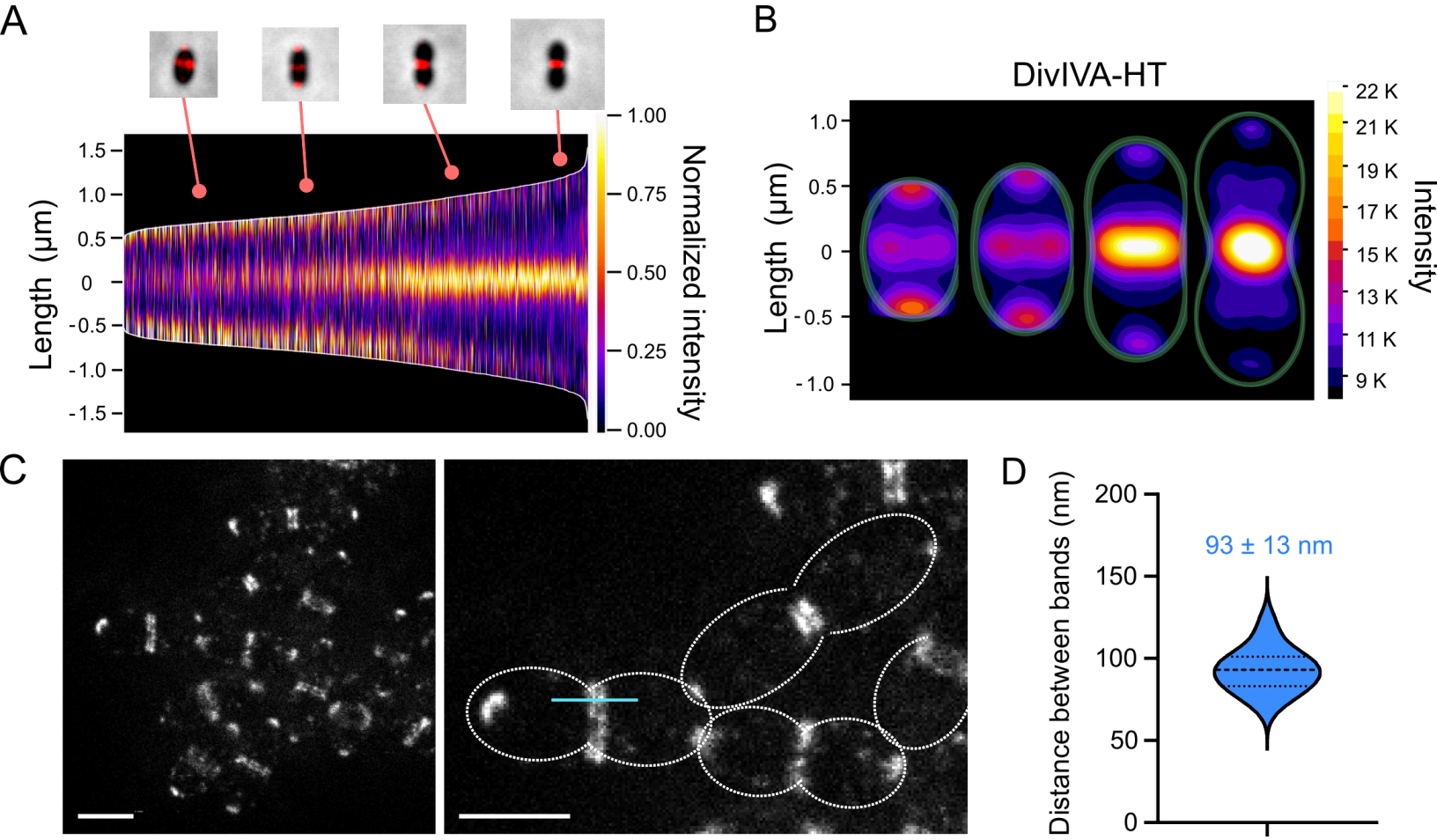
A
Length (µm)
1.5
1.0
0.5
0
-0.5
-1.0
-1.5
1.00
0.75
0.50
0.25
0.00
Normalized intensity
B
DivIVA-HT
Length (µm)
1.0
0.5
0
-0.5
-1.0
22 K
21 K
19 K
17 K
15 K
13 K
11 K
9 K
Intensity
C
D
Distance between bands (nm)
200
150
100
50
0
93 ± 13 nm

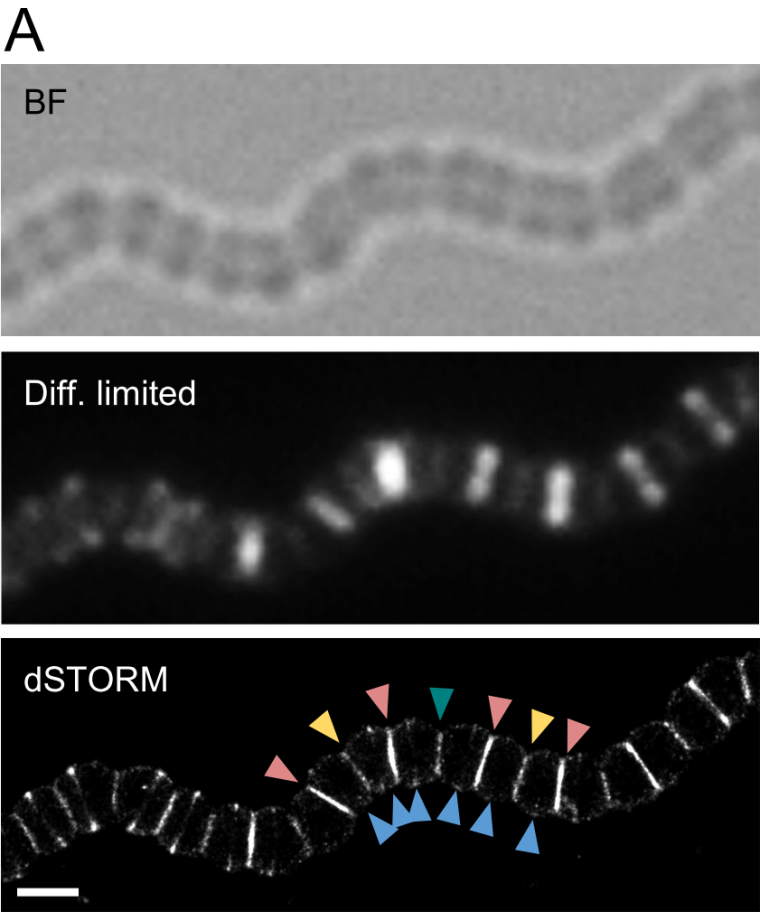
A
BF
Diff. limited
dSTORM

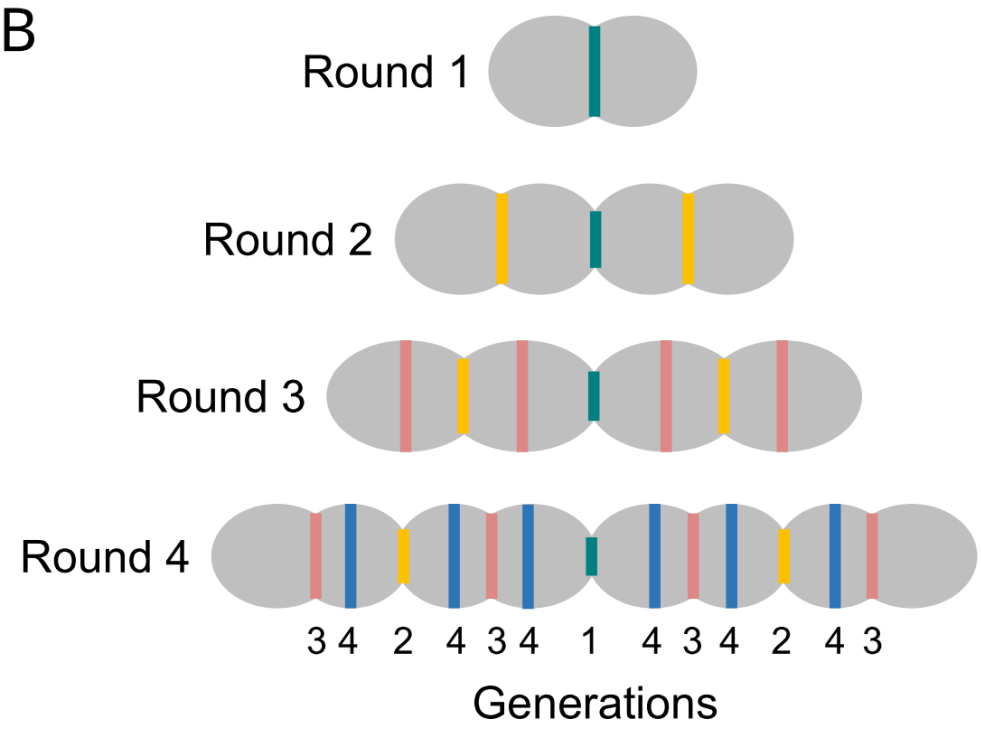
B
Round 1
Round 2
Round 3
Round 4
3 4 2 4 3 4 1 4 3 4 2 4 3
Generations

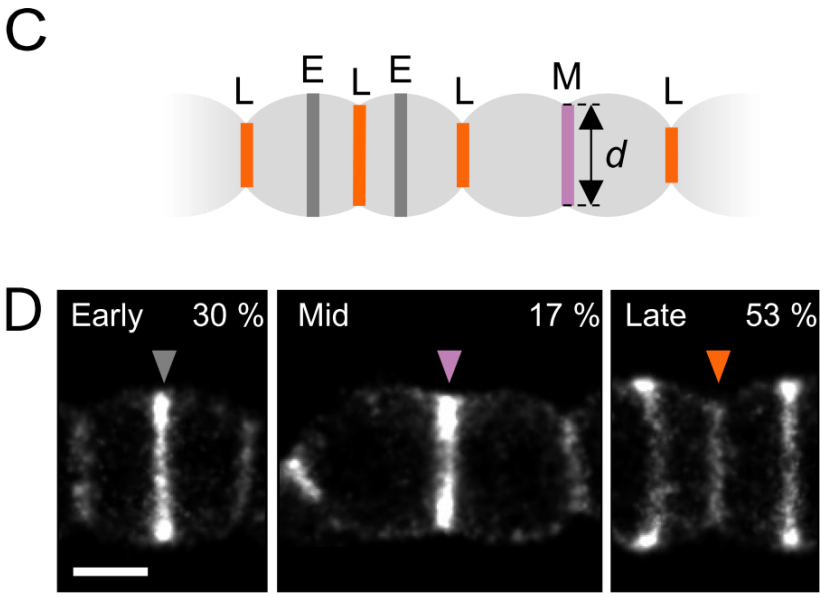
C
L
E
L
E
L
M
L
d
D
Early 30 %
Mid 17 %
Late 53 %

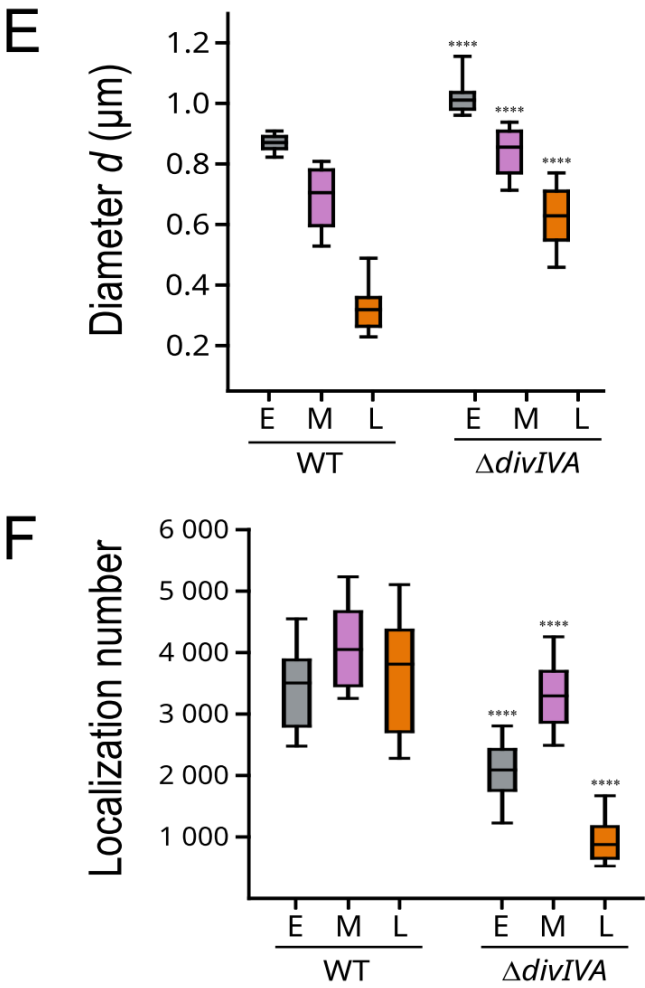
E
Diameter d (µm)
1.2
1.0
0.8
0.6
0.4
0.2
E M L
WT
E M L
ΔdivIVA
F
Localization number
6 000
5 000
4 000
3 000
2 000
1 000
E M L
WT
E M L
ΔdivIVA

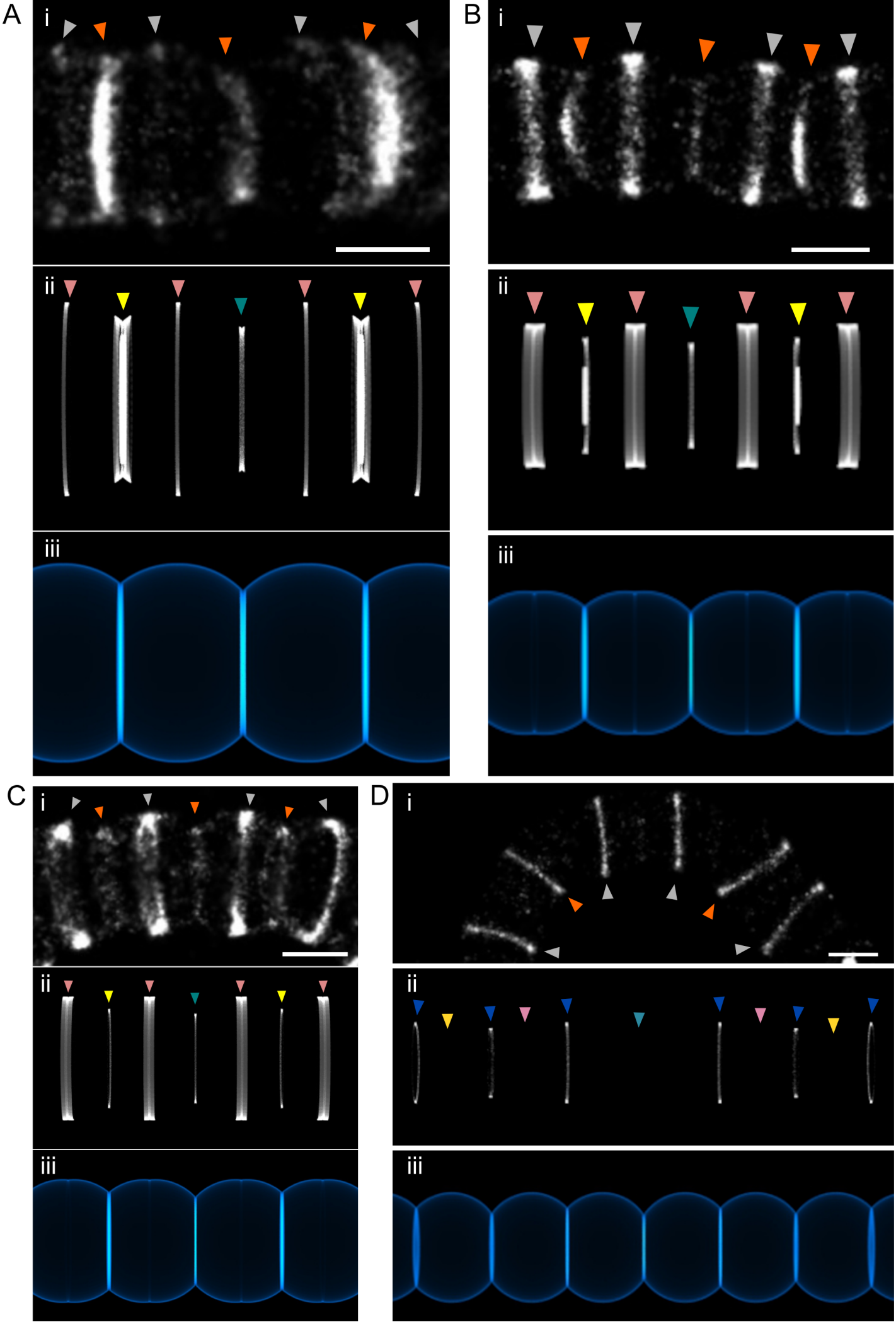
A
i
ii
iii
B
i
ii
iii
C
i
ii
iii
D
i
ii
iii

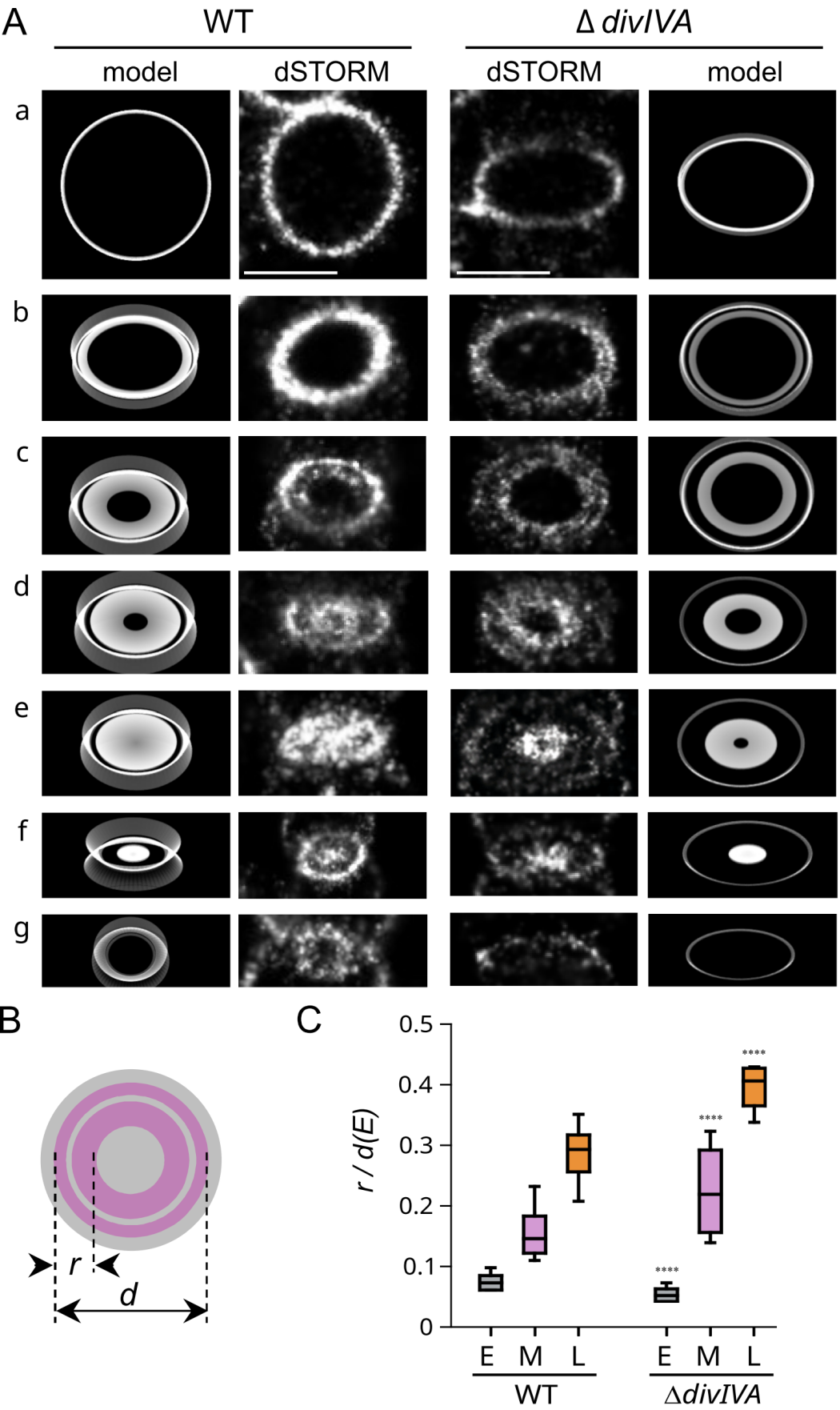
A
WT
Δ divIVA
model
dSTORM
dSTORM
model
a
b
c
d
e
f
g
B
r
d
C
r / d(E)
0.5
0.4
0.3
0.2
0.1
0
****
****
****
E M L
E M L
WT
ΔdivIVA

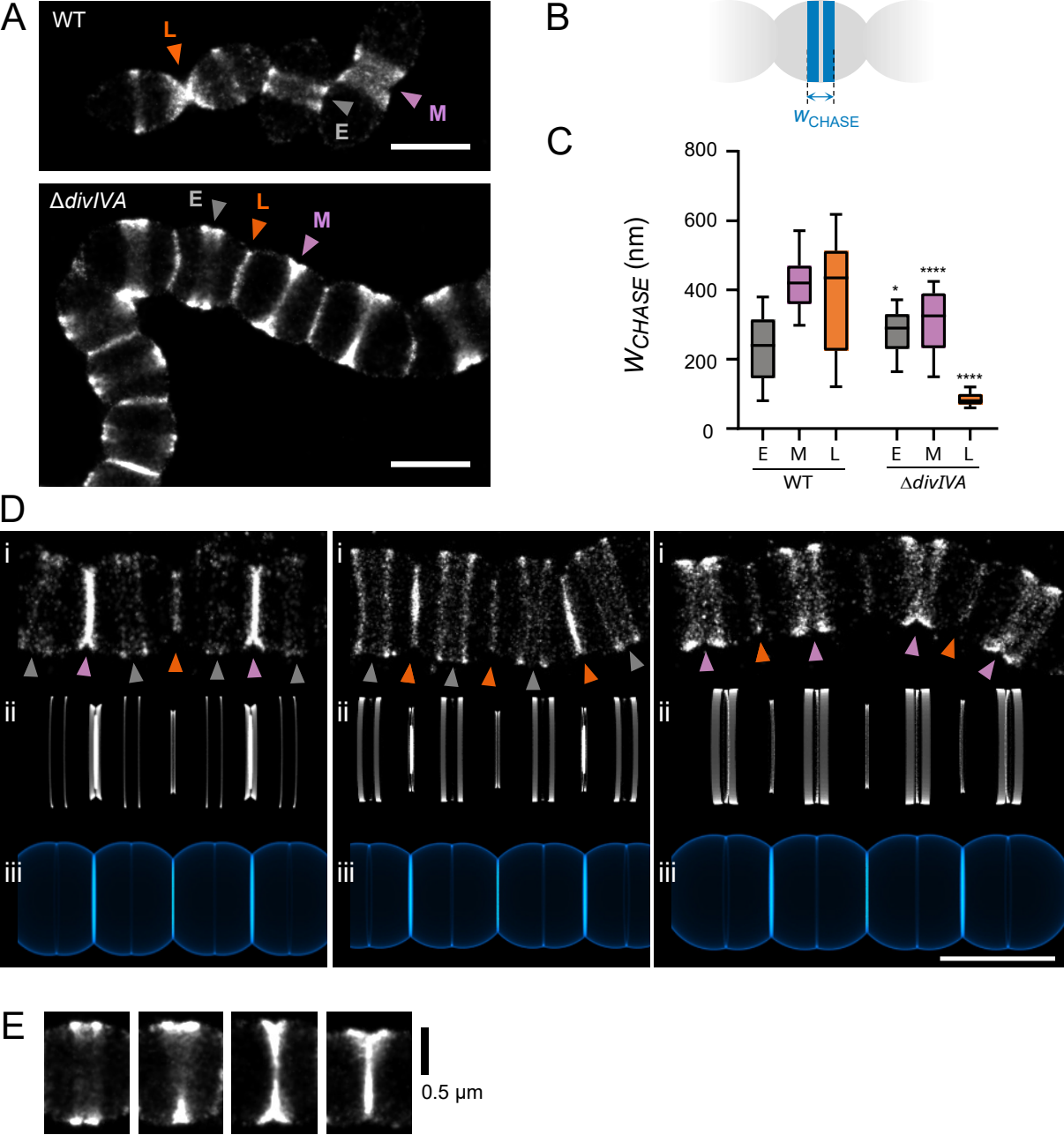
A
WT
L
E
M
ΔdivIVA
E
L
M
B
w_{CHASE}
C
800
600
400
200
0
w_{CHASE} (nm)
*
****
****
E
M
L
E
M
L
WT
ΔdivIVA
D
i
ii
iii
i
ii
iii
i
ii
iii
E
0.5 µm

A

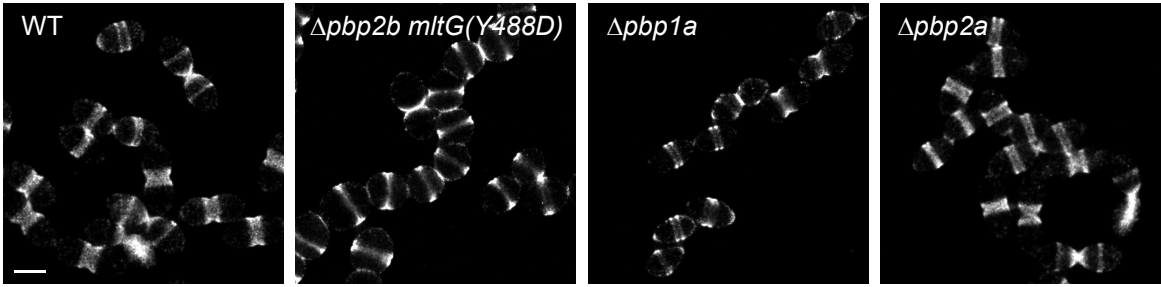
WT
Δpbp2b mltG(Y488D)
Δpbp1a
Δpbp2a

B

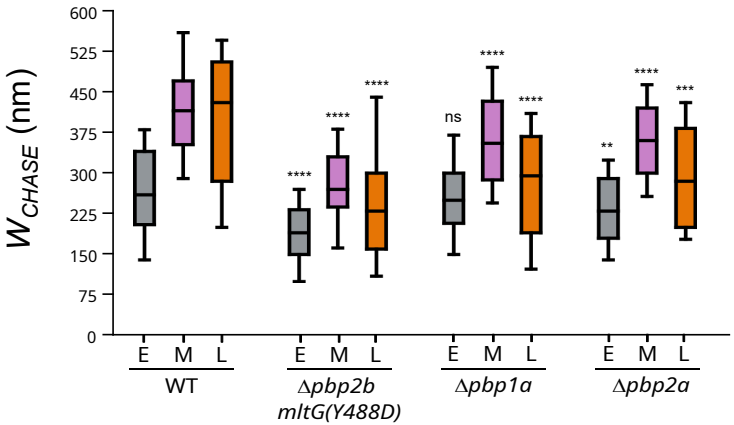
W_{CHASE} (nm)
600
525
450
375
300
225
150
75
0
****
****
****
ns
****
****
**
****
***
E M L
WT
E M L
Δpbp2b mltG(Y488D)
E M L
Δpbp1a
E M L
Δpbp2a

C

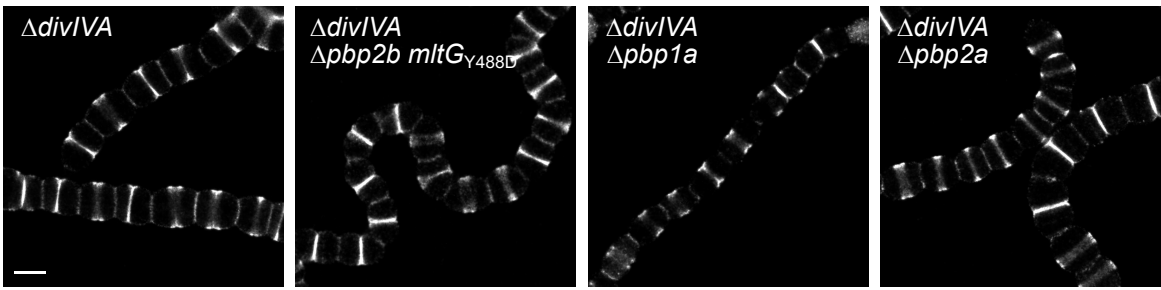
ΔdivIVA
ΔdivIVA Δpbp2b mltG$_{Y488D}$
ΔdivIVA Δpbp1a
ΔdivIVA Δpbp2a

D

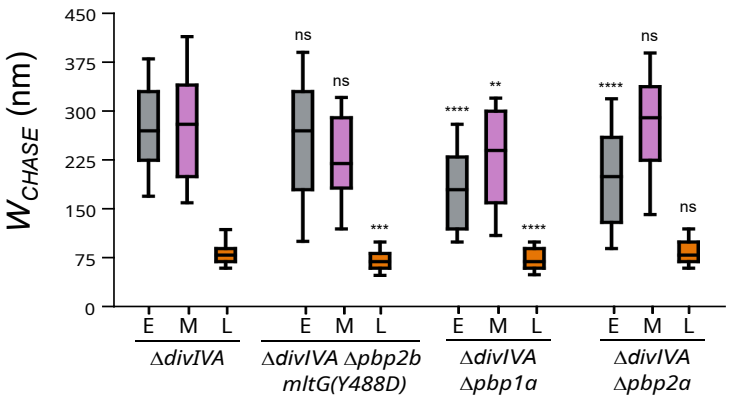
W_{CHASE} (nm)
450
375
300
225
150
75
0
ns
ns
***
****
**
****
****
ns
ns
E M L
ΔdivIVA
E M L
ΔdivIVA Δpbp2b mltG(Y488D)
E M L
ΔdivIVA Δpbp1a
E M L
ΔdivIVA Δpbp2a

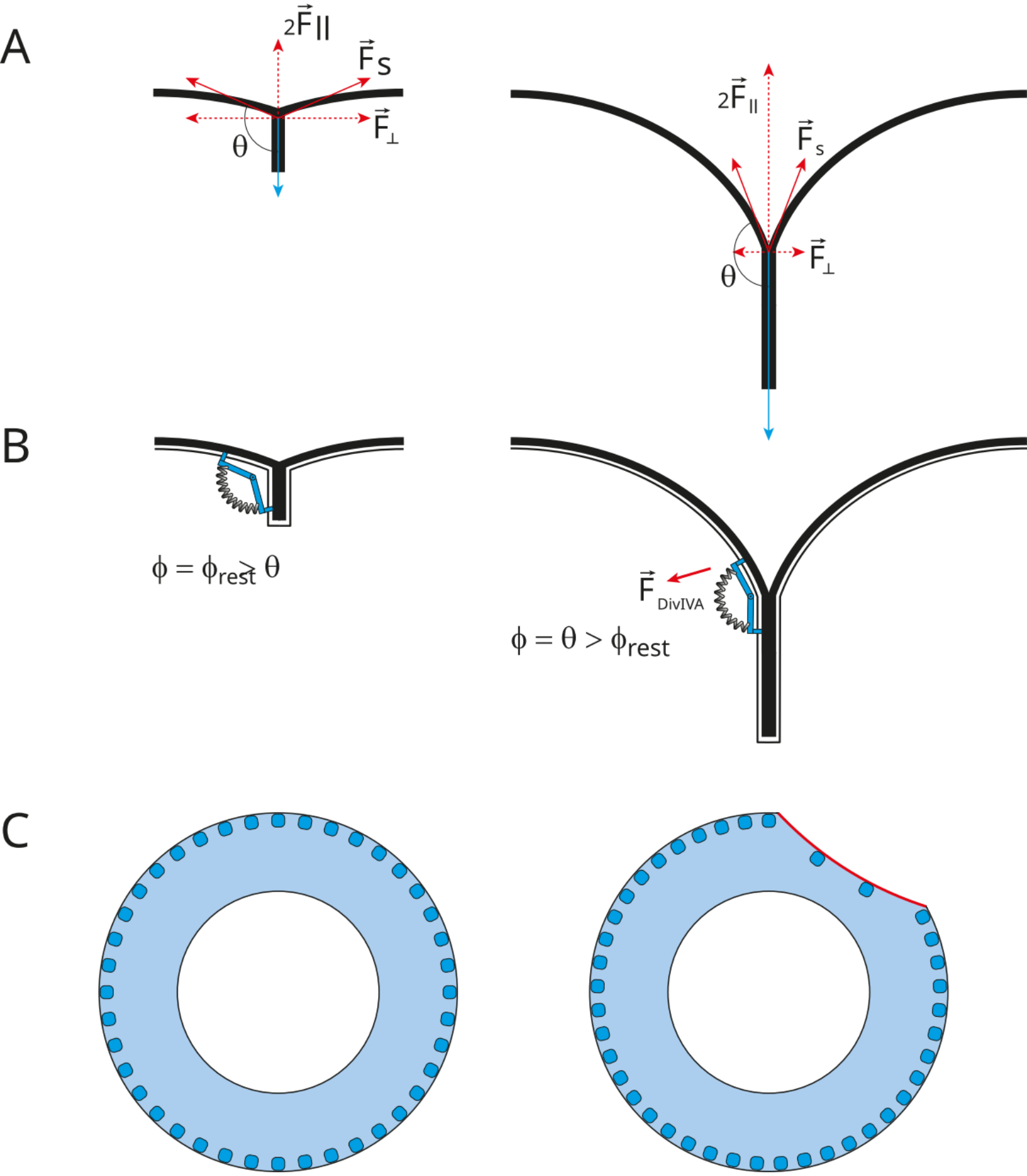
A
$2\vec{F}_{\parallel}$
$\vec{F}_S$
$\vec{F}_{\perp}$
θ
$2\vec{F}_{\parallel}$
$\vec{F}_s$
$\vec{F}_{\perp}$
θ
B
$\phi = \phi_{rest} > \theta$
$\vec{F}_{DivIVA}$
$\phi = \theta > \phi_{rest}$
C